

Identification of the partial differential equations governing microstructure evolution in materials: Inference over incomplete, sparse and spatially non-overlapping data

Z. Wang*, X. Huan[†] and K. Garikipati[‡]

June 14, 2022

Abstract

Pattern formation is a widely observed phenomenon in diverse fields including materials physics, developmental biology, ecology and atmospheric weather, among many others. The physics underlying the patterns is specific to the mechanisms operating in each field, and is encoded by partial differential equations (PDEs). With the aim of discovering hidden physics, we have previously presented a variational approach to identifying such systems of PDEs in the face of noisy data at varying fidelities (*Computer Methods in Applied Mechanics and Engineering*, **353**, 201-216, 2019). Here, we extend our methods to address the challenges presented by image data on microstructures in materials physics. PDEs are formally posed as initial and boundary value problems over combinations of time intervals and spatial domains whose evolution is either fixed or can be tracked. However, the heat treatments necessary to attain the kinetic rates and thermodynamic driving forces that result in significant evolution of microstructure in materials as well as the processing required for the microscopy that follows translate to notably different characteristics in the data so obtained. The vast majority of microscopy techniques for evolving microstructure in a given material system deliver micrographs of pattern evolution wherein the domain at one instant bears no spatial correlation to that at another time. This extends to boundary data, when available. The temporal resolution can rarely capture the fastest time scales that dominate the early dynamics, and noise abounds. Finally data for evolution of the same phenomenon in a material system may well be obtained from different physical samples. Against this backdrop of uncorrelated, sparse and multi-source data, we exploit the variational framework to make judicious choices of moments of fields and identify PDE operators from the dynamics. This step is preceded by an imposition of consistency to parsimoniously infer

*Department of Mechanical Engineering, University of Michigan

[†]Department of Mechanical Engineering, Michigan Institute for Computational Discovery & Engineering, University of Michigan, University of Michigan

[‡]Departments of Mechanical Engineering, and Mathematics, Michigan Institute for Computational Discovery & Engineering, University of Michigan, corresponding author, krishna@umich.edu

a minimal set of the spatial operators at steady state. The framework is demonstrated on synthetic data that reflects the characteristics of the experimental material microscopy images.

1 Introduction

Pattern-formation is ubiquitous in many branches of the physical sciences. It occurs prominently in material microstructures driven by diffusion, reaction and phase transformations, and is revealed by a range of microscopy techniques that delineate the components or constituent phases. In developmental biology, the examples include the organization of cells in the early embryo, markings on animal coats, insect wings, plant petals and leaves, as well as the segregation of cell types during the establishment of tissues. In ecology, patterns are formed on larger scales as types of vegetation spreads across forests. For context, we briefly discuss the role of pattern forming systems of equations in these phenomena. Pattern formation during phase transformations in materials physics can happen as the result of instability-induced bifurcations from a uniform composition [1, 2, 3], which was the original setting of the Cahn-Hilliard treatment. Following Alan Turing’s seminal work on reaction-diffusion systems [4], a robust literature has developed on the application of nonlinear versions of this class of PDEs to model pattern formation in developmental biology [5, 6, 7, 8, 9, 10, 11, 12, 13]. The Cahn-Hilliard phase field equation [14] has also been applied to model other biological processes with evolving fronts, such as tumor growth and angiogenesis [15, 16, 17, 18, 19, 20, 21, 22]. Reaction-diffusion equations also appear in ecology, where they are more commonly referred to as activator-inhibitor systems, and are found to underlie large scale patterning [23, 24]. All of these pattern forming systems fall into the class of nonlinear, parabolic PDEs, and have spawned a vast literature in mathematical physics. They can be written as systems of first-order dynamics driven by a number of time-independent terms of algebraic and differential form. The spatio-temporal, differentio-algebraic operators act on either a composition (normalized concentration) or an order parameter. It also is common for the algebraic and differential terms to be coupled across multiple species.

Patterns in physical systems are of interest because, up to a point, human experts in each of the above fields (materials microscopists, developmental biologists, ecologists and meteorologists) are able to identify phenomena solely on the basis of patterns. This success of intuition fed by experience does, however, break down when, for instance, the materials scientist is confronted by the dynamic processes in an unstudied alloy, or the developmental biologist considers a previously neglected aspect of morphogenesis. In such settings the challenge is to discover the operative physics from among a range of mechanisms. As with all of quantitative physics, the only rigorous route to such discovery is the mathematical one. For systems that vary over space and time, this description is in the form of partial differential equations (PDEs). Identification of participating PDE operators from spatio-temporal observations can thus uncover the underlying physical mechanisms, and lead to improved understanding, prediction, and manipulation of these systems.

Distinct from classical adjoint-based approaches to inverse problems, the system identification problem on PDEs is to balance accuracy and complexity in finding the best model among many possible candidates that could explain the spatio-temporal data on the dynamical system. The proposed models can be parameterized by the coefficients of candidate operators, which serve as a basis. The task of solving this inverse problem can then be approached as an optimization problem to find the best coefficient values that minimize a pre-defined loss function. The principle that parsimony of physical mechanisms is favored translates to sparsity of the coefficients. The loss function may be defined in two ways by considering: (a) how well the results predicted from the identified model match the real data, which is ideally posed in a Bayesian setting, or (b) how well the real data satisfies the identified model, which leads to regression-based methods. The first approach requires many forward solutions of the PDE models, which is computationally expensive and has the potential to become infeasible due to the curse of dimensionality. Inference of a fixed number of coefficients in specified PDE models is the central feature of methods such as Markov Chain Monte Carlo and PDE-constrained optimization with adjoints (references needed). With these methods, identifying the best model from a large candidate set remains challenging. However, they have significant flexibility in treating the data, which could be sparse, only available over some subset of the domain, collected at a few time steps, some statistical measures or other *Quantities of Interests* (QoIs). In the second approach (b) the PDEs themselves have to be represented by the data, which can be achieved by constructing the operators either in strong form such as finite difference, as in the Sparse Identification of Nonlinear Dynamics (SINDY) approach [25]), or in weak form built upon basis functions, as in the Variational System Identification (VSI) approach [26]. Both representations pose stringent requirements on the data for accurately constructing the operators. The first of these is the need for time series data that can be related to chosen spatial points either directly or by interpolation. This is essential for consistency with a PDE that is written in terms of spatio-temporal operators at defined points in space and instants in time dependent. The second requirement is for data with sufficient spatial resolution to construct spatial differential operators of possibly high order. However approach (b) enjoys the advantage that repeated forward PDE solutions are not necessary. PDE operators have thus been successfully identified from a comprehensive library of candidates [25, 26, 27, 28]. In a different approach to solving inverse problems [29], the strong form of a specified PDE was directly embedded in the loss function while training deep neural network representations of the solution variable. However, this approach depends on data at high spatial and temporal resolution for successful training of the deep neural network representations of the solution variable.

A significant discordance can exist in the form of material microstructure datasets when juxtaposed against the underlying premise of all the above approaches. These experimental datasets, while corresponding to different times are also commonly collected at different sub-domains (including scenarios of completely non-overlapping spatial regions) of a sample at each instant. Further-

more, while subject to the same processing conditions, they may well come from different physical sample specimen. This is because the experimental techniques for extracting data at a given time after sample preparation (which can include mechanical, chemical and thermal steps) involve a destructive processing including cutting and grinding of the specimen. After this procedure, the entire specimen is removed from further experimentation, and a new specimen needs to be created if data is to be collected at a different incubation time. Both these conditions essentially negate the foundational feature of a PDE describing the temporal evolution of quantities at chosen spatial points for a single instantiation of that initial and boundary value problem. The spatial sub-domains on which microscopy is conducted may represent only small portions of entire samples. Boundary data, if present, are also prey to the above loss of spatial localization over time. Finally, the effort of processing (sample preparation and heat treatment) to attain the desired kinetic rates and thermodynamic driving forces, and subsequently to obtain microscopy images leads to sparsity of data in time; even tens of instants are uncommon.

In this communication, we extend our Variational System Identification methods [26] to uncorrelated, sparse and multi-source data, motivated by the above challenges of experimental microscopy in materials physics. The goal remains to discover the physical mechanisms underlying patterns of diffusion, reaction and phase transformation in materials physics. Imposition of consistency on the steady state versions of candidate PDEs opens the door to parsimonious choice of a minimal set of spatial operators. We present novel advances that exploit the variational framework and statistical similarity to cast the spatial problem in terms of moments and circumvent the loss of spatial correlation. This sequence of steps renders temporally sparse data to be sufficient for inferring the kinetics. These methods are described in Section 2 and demonstrated on synthetic data in Section 3. A discussion and conclusions are presented in Section 4.

2 Identification of PDEs from spatially non-overlapping and sparse data

2.1 System identification and the Galerkin weak form

We first provide a brief discussion of how the weak form of PDEs will be used in this work. We start with the general strong form for first-order dynamics written as

$$\frac{\partial C}{\partial t} - \boldsymbol{\chi} \cdot \boldsymbol{\omega} = 0, \quad (1)$$

where $\boldsymbol{\chi}$ is a vector containing all possible independent terms expressed as algebraic and differential operators on the scalar solution C :

$$\boldsymbol{\chi} = [1, C, C^2, \dots, \nabla^2 C, \dots], \quad (2)$$

and ω is the vector of scalar coefficients from in front of each term. For example, using this nomenclature, the one-field diffusion reaction equation

$$\frac{\partial C}{\partial t} - D\nabla^2 C - f = 0 \quad (3)$$

with constant diffusivity D and reaction rate f has

$$\chi = [1, C, C^2, \nabla^2 C] \quad \text{and} \quad \omega = [f, 0, 0, D]. \quad (4)$$

Note that the time derivative $\partial C/\partial t$ is treated separately from the other terms in order to highlight the first-order dynamics of the problems that we target in this work.

Our system identification problem entails finding the correct data-generating coefficient vector ω from among a dictionary of candidate operators χ given some observational data of the dynamical system.

As argued by Wang et al. [26], the weak form offers particular advantages for the system identification problem: It allows the use of basis functions that can be drawn from function classes that have higher-order regularity. Furthermore, the weak form transfers spatial derivative operators from the trial solution, represented by the data, to the weighting function. These two features significantly mollify the noise, stiffness and general loss of robustness associated with constructing spatial derivatives on the data. They are especially relevant for the consideration of high-order gradient operators on the data, which can be relevant for many types of pattern-forming phenomena in physics.

For infinite-dimensional problems with Dirichlet boundary conditions on Γ^c , the weak form is obtained by first stating: $\forall w \in \mathcal{V}$ where $\mathcal{V} = \{w \mid w = 0 \text{ on } \Gamma^c\}$, find $C \in \mathcal{S}$ where $\mathcal{S} = \{C \mid C = \bar{C} \text{ on } \Gamma^c\}$ such that

$$\int_{\Omega} w \left(\frac{\partial C}{\partial t} - \chi \cdot \omega \right) dv = 0. \quad (5)$$

Integration by parts and the application of Dirichlet boundary conditions, which are determined by the actual operators χ lead to the final weak form, which we do not state here for each instance of χ . For finite-dimensional fields C^h, w^h replacing C, w , respectively, we have $C^h \in \mathcal{S}^h \subset \mathcal{S}$ where $\mathcal{S}^h = \{C^h \in \mathcal{H}^2(\Omega) \mid C^h = \bar{C} \text{ on } \Gamma^u\}$, such that $\forall w^h \in \mathcal{V}^h \subset \mathcal{V}$ where $\mathcal{V}^h = \{w^h \in \mathcal{H}^2(\Omega) \mid w^h = 0 \text{ on } \Gamma^u\}$. The choice of $\mathcal{H}^2(\Omega)$ as the Sobolev space is motivated by the differential operators, which reach the highest order of two in the weak forms we consider (four in strong form). The variations w^h and trial solutions C^h are defined component-wise using a finite number of basis functions,

$$w^h = \sum_{a=1}^{n_b} d^a N^a \quad (6)$$

$$C^h = \sum_{a=1}^{n_b} c^a N^a, \quad (7)$$

where n_b is the dimensionality of the function spaces \mathcal{S}^h and \mathcal{Y}^h , and N^a represents the basis functions.

If, at each time instant of interest, t , the data available are in the form $C(\mathbf{x}_I, t)$ for $I = 1, \dots, n_{\text{sp}}$ and n_{sp} being the number of spatial points such that $\mathbf{x}_I \in \Omega$, then the approach of Variational System Identification by Wang et al. [26] presents itself as a powerful approach. However, as explained in the Introduction, the combination of sample processing and microscopy techniques implies that the data acquired at each time, which we call a snapshot, are only available over subdomains of the full field that do not correspond to the same spatial locations—i.e., are spatially non-overlapping (Figure 1). Furthermore, each snapshot is usually produced from a different physical specimen due to the destructive and intrusive nature of data acquisition in the experiments. We next present a moments-based approach that exploits the variational setting.

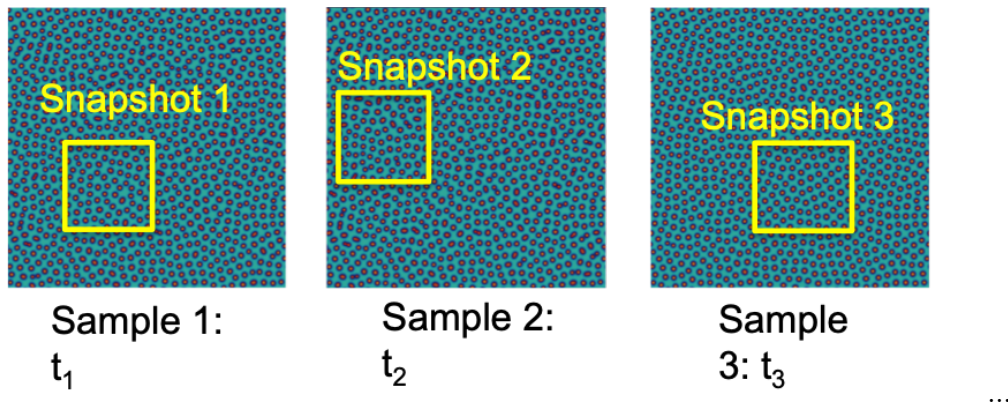


Figure 1: The sample data shown within the snapshots corresponding to each time instant, are only available over sub-domains of the full field. They are spatially uncorrelated over time.

2.2 Method of moments

In statistics, the *method of moments* is an approach to estimate a population’s parameters by matching the moments estimated from sample data. The dynamical system characterizes the distribution $f_W|_n(w^i; \boldsymbol{\omega})$ of the total mass, regarded here as a random variable W at time t_n . We note that W is obtained from the random field C , which is governed by the PDE we seek, as shown below. It represents the first moment of C . We show below that the first k moments of the true spatial distribution can be expressed as functions of the coefficient $\boldsymbol{\omega}$ given the full field data, $C(\mathbf{x}, t_n)$, of the dynamical system:

$$E[W|_n] = g_1(C_n, \boldsymbol{\omega}), \quad E[W_2|_n] = g_2(C_n, \boldsymbol{\omega}), \dots, \quad E[W_k|_n] = g_k(C_n, \boldsymbol{\omega}) \quad (8)$$

where $E[\bullet]$ denotes the expected value defined by

$$E[W_k|_n] := \int_{\Omega} C_n^k dv = g_k(C_n, \boldsymbol{\omega}), \quad (9)$$

where the second equality defining the functional g_k is determined by the candidate PDE, as shown below. These moments of the true distribution can be estimated from the sample data (i.e., partial field) \widehat{C}_n such that:

$$E[W|_n] \approx g_1(\widehat{C}_n, \boldsymbol{\omega}), \quad E[W_2|_n] \approx g_2(\widehat{C}_n, \boldsymbol{\omega}), \dots, \quad E[W_k|_n] \approx g_k(\widehat{C}_n, \boldsymbol{\omega}). \quad (10)$$

The coefficient vector $\boldsymbol{\omega}$ can be estimated as the regression solution to the above equations at multiple time steps:

$$\begin{array}{ccccccc} \dots & & \dots & & \dots & & \dots \\ E[W|_{n-1}] = g_1(\widehat{C}_{n-1}, \boldsymbol{\omega}), & E[W^2|_{n-1}] = g_2(\widehat{C}_{n-1}, \boldsymbol{\omega}), & \dots, & E[W^k|_{n-1}] = g_k(\widehat{C}_{n-1}, \boldsymbol{\omega}) & & & \\ E[W|_n] = g_1(\widehat{C}_n, \boldsymbol{\omega}), & E[W^2|_n] = g_2(\widehat{C}_n, \boldsymbol{\omega}), & \dots, & E[W^k|_n] = g_k(\widehat{C}_n, \boldsymbol{\omega}) & & & (11) \\ E[W|_{n+1}] = g_1(\widehat{C}_{n+1}, \boldsymbol{\omega}), & E[W^2|_{n+1}] = g_2(\widehat{C}_{n+1}, \boldsymbol{\omega}), & \dots, & E[W^k|_{n+1}] = g_k(\widehat{C}_{n+1}, \boldsymbol{\omega}) & & & \\ \dots & & \dots & & \dots & & \dots \end{array}$$

We note that this approach assumes the existence of moments being considered (e.g., that they are finite), and that the partial field can be appropriately interpreted as a sample of the full field.

In this work, we consider only the first and second moments of the concentration field. These can be interpreted as the volume averaged concentration field, and volume averaged square of the concentration field. They both are special cases of choosing a specific weighting functions in the weak form (5). We present a two-stage procedure to estimate the coefficients.

First, we rewrite Equation (5) with operators $\boldsymbol{\chi}$ and coefficients $\boldsymbol{\omega}$ split into two parts, and the entire equation divided by the volume:

$$\frac{1}{V} \int_{\Omega} w \left(\frac{\partial C}{\partial t} - (\boldsymbol{\chi}_1 \cdot \boldsymbol{\omega}_1 + \boldsymbol{\chi}_2 \cdot \boldsymbol{\omega}_2) \right) dv = 0. \quad (12)$$

where $\boldsymbol{\chi}_1$ contains all non-gradient dependent operators, $\boldsymbol{\chi}_2$ contains all gradient dependent operators such as:

$$\boldsymbol{\chi}_1 = [1, C, C^2, \dots], \quad \boldsymbol{\chi}_2 = [\nabla^2 C, \nabla \cdot C \nabla C, \nabla^4 C, \dots] \quad (13)$$

and $\boldsymbol{\omega}_1$ and $\boldsymbol{\omega}_2$ are the vectors of corresponding coefficients. We write a backward difference approximation of the time derivative. Choosing $w = 1$, after integrating by parts, we have:

$$\frac{1}{V} \int_{\Omega} C_n dv = \frac{1}{V} \Delta t \int_{\Omega} \boldsymbol{\chi}_1 dv \cdot \boldsymbol{\omega}_1 + \frac{1}{V} \int_{\Omega} C_{n-1} dv \quad (14)$$

at time t_n . All gradient dependent operators vanish since the gradients are transferred to the constant weighting function.

Next, we choose $w = C_n$, we have:

$$\frac{1}{V} \int_{\Omega} C_n \frac{\partial C_n}{\partial t} dv = \frac{1}{V} \int_{\Omega} C_n \boldsymbol{\chi} \cdot \boldsymbol{\omega} dv \quad (15)$$

$$\frac{1}{V} \int_{\Omega} \frac{1}{2} \frac{\partial C_n^2}{\partial t} dv = \frac{1}{V} \int_{\Omega} C_n \boldsymbol{\chi} \cdot \boldsymbol{\omega} dv \quad (16)$$

$$= \frac{1}{V} \int_{\Omega} C_n \boldsymbol{\chi}_1 \cdot \boldsymbol{\omega}_1 dv + \frac{1}{V} \int_{\Omega} C_n \boldsymbol{\chi}_2 \cdot \boldsymbol{\omega}_2 dv \quad (17)$$

Again writing a backward difference approximation of the time derivative:

$$\frac{1}{V} \int_{\Omega} C_n^2 dv = \frac{1}{V} 2\Delta t \left(\int_{\Omega} C \boldsymbol{\chi}_1 dv \cdot \boldsymbol{\omega}_1 - \int_{\Omega} \nabla C \cdot \tilde{\boldsymbol{\chi}}_2 dv \cdot \boldsymbol{\omega}_2 \right) + \int_{\partial\Omega} C \tilde{\boldsymbol{\chi}}_2 \cdot \mathbf{n} ds + \frac{1}{V} \int_{\Omega} C_{n-1}^2 dv \quad (18)$$

where, $\nabla \cdot \tilde{\boldsymbol{\chi}}_2 := \boldsymbol{\chi}_2$ is a divergence relation. Here we assume that the net influx on the boundary vanishes. This is typically true for experiments in which there is no flux across the sample boundaries. Consequently we can eliminate the boundary terms in the weak forms above to write:

$$\frac{1}{V} \int_{\Omega} C_n^2 dv = \frac{1}{V} 2\Delta t \left(\int_{\Omega} C \boldsymbol{\chi}_1 dv \cdot \boldsymbol{\omega}_1 - \int_{\Omega} \nabla C \cdot \tilde{\boldsymbol{\chi}}_2 dv \cdot \boldsymbol{\omega}_2 \right) + \frac{1}{V} \int_{\Omega} C_{n-1}^2 dv \quad (19)$$

Given full field data, the two moments (Equation 14 and 18) can be evaluated over the same sub domain $\hat{\Omega}$, where $\hat{V} = \text{Vol}(\hat{\Omega})$:

$$\frac{1}{\hat{V}} \int_{\hat{\Omega}} C_n dv = \frac{1}{\hat{V}} \Delta t \int_{\hat{\Omega}} \boldsymbol{\chi}_1 dv \cdot \boldsymbol{\omega}_1 + \frac{1}{\hat{V}} \int_{\hat{\Omega}} C_{n-1} dv \quad (20)$$

$$\frac{1}{\hat{V}} \int_{\hat{\Omega}} C_n^2 dv = \frac{1}{\hat{V}} 2\Delta t \left(\int_{\hat{\Omega}} C_n \boldsymbol{\chi}_1 dv \cdot \boldsymbol{\omega}_1 - \int_{\hat{\Omega}} \nabla C_n \cdot \tilde{\boldsymbol{\chi}}_2 dv \cdot \boldsymbol{\omega}_2 \right) + \frac{1}{\hat{V}} \int_{\hat{\Omega}} C_{n-1}^2 dv \quad (21)$$

Here we also assume that the boundary flux is balanced out over the sub domain $\hat{\Omega}$.

Now we make our first key assumption that the volume-normalized first and second moments of C_n over subdomain, $\hat{\Omega}$, can be approximated by the corresponding volume-normalized moments evaluated over different subdomains. This reflects the assumption that the data over each of these subdomains are statistically similar, so that volume-normalization results in approximate equality:

First key assumption: Volume-normalized moments are approximately equal due to statistical similarity of data over different subdomains Ω_n .

$$\frac{1}{\hat{V}} \int_{\hat{\Omega}} C_n dv \approx \frac{1}{\hat{V}_n} \int_{\hat{\Omega}_n} C_n dv \quad (22)$$

and

$$\frac{1}{\hat{V}} \int_{\hat{\Omega}} C_n^2 dv \approx \frac{1}{\hat{V}_n} \int_{\hat{\Omega}_n} C_n^2 dv \quad (23)$$

This assumption allows us to use data collected from different subdomains at different times to estimate the volume-normalized moments by replacing the integration in Equations (20) and (21), over the same subdomain $\widehat{\Omega}$ by integrations over the subdomains that correspond to the relevant times:

$$\frac{1}{\widehat{V}_n} \int_{\widehat{\Omega}_n} C_n dv \approx \frac{1}{\widehat{V}_n} \Delta t \int_{\widehat{\Omega}_n} \chi_1 dv \cdot \omega_1 + \frac{1}{\widehat{V}_{n-1}} \int_{\widehat{\Omega}_{n-1}} C_{n-1} dv \quad (24)$$

$$\frac{1}{\widehat{V}_n} \int_{\widehat{\Omega}_n} C_n^2 dv \approx \frac{1}{\widehat{V}_n} 2\Delta t \left(\int_{\widehat{\Omega}_n} C_n \chi_1 dv \cdot \omega_1 - \int_{\widehat{\Omega}_n} \nabla C_n \cdot \tilde{\chi}_2 dv \cdot \omega_2 \right) + \frac{1}{\widehat{V}_{n-1}} \int_{\widehat{\Omega}_{n-1}} C_{n-1}^2 dv \quad (25)$$

We then make our second key assumption that the volume-normalized first and second moments of C over sub domains that correspond to the relevant times can be approximated by the corresponding volume-normalized moments evaluated using data, \tilde{C} , collected from different samples at the relevant times. (Here, the tilde denotes data from a different sample.) In experiments, data from different samples are measured under the same conditions, and statistical similarity between samples is assumed. The mathematical and numerical equivalence to this procedure is modeled by employing the same initial condition with different spatially randomized perturbations. This is explained in detail in Section 3.1.

Second key assumption: Volume-normalized moments are approximated using data, \tilde{C} , from different samples.

$$\frac{1}{\widehat{V}_n} \int_{\widehat{\Omega}_n} \widehat{C}_n dv \approx \frac{1}{\widehat{V}_n} \int_{\widehat{\Omega}_n} \overline{C}_n dv \quad (26)$$

and

$$\frac{1}{\widehat{V}_n} \int_{\widehat{\Omega}_n} \widehat{C}_n^2 dv \approx \frac{1}{\widehat{V}_n} \int_{\widehat{\Omega}_n} \overline{C}_n^2 dv \quad (27)$$

This assumption allows us to use data collected from different samples.

The two key approximations are in fact based on the assumption that due to statistical similarity across a sample and between samples, the data over different sub domains from different samples can represent the whole data set. This is the same foundational principle underlying the experimental techniques, allowing the consideration of a sub domain to represent the entire field. Noting that the entire domain Ω itself is a subdomain, Equations (22)-(27) also hold over Ω , provided there is no net boundary flux on $\partial\Omega$ and that the effects of spatially randomized perturbations are dissipated away by the dynamics. The data collected from pattern forming physics better satisfies the assumption of statistical similarity for larger subdomains because localized features are averaged out better?. The statistical similarity of the data is discussed in the Section 3.2. Replacing the approximations

by equalities, Equation (24) and (25) can be re-written to be:

$$\text{Stage 1:} \quad \frac{1}{\Delta t} \left(\frac{1}{\widehat{V}_n} \int_{\widehat{\Omega}_n} C_n dv - \frac{1}{\widehat{V}_{n-1}} \int_{\widehat{\Omega}_{n-1}} C_{n-1} dv \right) = \frac{1}{\widehat{V}_n} \int_{\widehat{\Omega}_n} \chi_1 dv \cdot \omega_1 \quad (28)$$

$$\text{Stage 2:} \quad \frac{1}{2\Delta t} \left(\frac{1}{\widehat{V}_n} \int_{\widehat{\Omega}_n} C_n^2 dv - \frac{1}{\widehat{V}_{n-1}} \int_{\widehat{\Omega}_{n-1}} C_{n-1}^2 dv \right) - \frac{1}{\widehat{V}_n} \int_{\widehat{\Omega}_n} C_n \chi_1 dv \cdot \omega_1 = \frac{1}{\widehat{V}_n} \int_{\widehat{\Omega}_n} \nabla C_n \cdot \tilde{\chi}_2 dv \cdot \omega_2 \quad (29)$$

Note that, without loss of generality, the data C could be from different samples. We define the left hand sides to be the target vectors and $\frac{1}{\widehat{V}_n} \int_{\widehat{\Omega}_n} \chi_1 dv$ and $-\frac{1}{\widehat{V}_n} \int_{\widehat{\Omega}_n} \nabla C \cdot \tilde{\chi}_2 dv$ to be the candidate basis operators.

Note the choice of the weighting function $w^h \in \mathcal{V}^h$ is arbitrary. For example, it could be constant or a function of the spatial position \mathbf{x} . However the judicious choice of w^h is critical for success of Variational System Identification. A spatially constant w^h eliminates all gradient dependent terms in the weak form and thus enables the identification of non-gradient terms in Stage 1. The choice of $w^h = C$ in Stage 2 makes the Laplace and Biharmonic operators into quadratic forms in weak form (see section 2.3 below). This is suitable for pattern forming dynamics, because it ensures that the integrand of $\int_{\Omega} \nabla C \cdot \nabla C dv$ is non-negative, and that the corresponding weak operators are identifiable. However certain choices of w^h could render some operators unidentifiable. For example, choosing $w = x_1$, the integral of $\nabla x_1 \cdot \nabla C$ is not significant in the pattern forming physics, since this term is cancelling out by the x_1 -symmetry of the particles as shown in Figure 1.

2.3 Candidate basis operators

Suppose we have data for the field C on certain degrees of freedom (DOFs) of a discretization for a series of time steps. These DOFs are the control variables if non-uniform rational B-spline basis functions are used. Using these DOFs, a Galerkin representation of the field could be constructed over the domain. Below we illustrate the procedure of generating candidate basis operators in weak form with three example terms.

Algebraic terms C^k at time t_n with $w = 1$:

$$\chi_1^{C^k} = \frac{1}{V_n} \int_{\Omega_n} C_n^k dv \quad (30)$$

Note the constant term, $\Xi_1^{C^0} = 1$, is invariant over time. All algebraic operators therefore appear in χ_1 which is multiplied by weighting function $w^h = 1$. All gradient-dependent operators, however, appear χ_2 which is multiplied by weighting function $w^h = C$.

Laplace operator $\nabla^2 C$ at time t_n with $w = C$: Multiplying by the weighting function and integrating by parts:

$$\int_{\Omega} C_n \nabla^2 C_n^h dv = - \int_{\Omega} \nabla C_n \cdot \nabla C_n^h dv \quad (31)$$

$$+ \int_{\Gamma} \nabla C_n^2 \cdot \mathbf{n} ds \quad (32)$$

Note that the second term on the right is the Neumann boundary term. We define the first term

$$\chi_2^{\nabla^2 C}|_n = - \int_{\Omega} \nabla C_n \cdot \nabla C_n^h dv \quad (33)$$

as the basis for $\nabla^2 C$.

Biharmonic operator $\nabla^4 C_n$ at time t_n with $w = C$: Multiplying by the weighting function and integrating by parts:

$$\begin{aligned} \int_{\Omega} w \nabla^4 C_n^h dv &= \int_{\Omega} \nabla^2 C_n^h \nabla^2 C_n^h dv \\ &- \int_{\Gamma} \nabla C_n^h \cdot \mathbf{n} \nabla^2 C_n^h ds \\ &+ \int_{\Gamma} C_n^h \nabla(\nabla^2 C_n^h) \cdot \mathbf{n} ds. \end{aligned} \quad (34)$$

We define the first term

$$\chi_2^{\nabla^4 C}|_n = \int_{\Omega} \nabla^2 C_n^h \nabla^2 C_n^h dv \quad (35)$$

as the basis for the biharmonic operator $\nabla^4 C$. The last two terms in (34) are, respectively, a higher-order Dirichlet boundary condition (as emerges from variational calculus applied in the context of the full equation [2]) and the Neumann boundary condition.

The second-order gradients in the Equation (35) require the solutions and basis functions to lie in $\mathcal{H}^2(\Omega)$, while the Lagrange polynomial basis functions traditionally used in finite element analysis only lie in $\mathcal{H}^1(\Omega)$. We therefore draw the basis functions, N , from the family of Non-Uniform Rational B-Splines (NURBS), and adopt Isogeometric Analysis (IGA) in our simulations to find the solutions in $\mathcal{H}^2(\Omega)$. A discussion of the NURBS basis and IGA is beyond the scope of this paper; interested readers are directed to the original works on this topic [30].

2.4 Identification of basis operators via two stage stepwise regression

To identify a dynamical system, we need to generate all possible basis operators, χ_1 and χ_2 , acting on the solution, compute the non-zero coefficient for each basis operator that is in the model

(relevant bases), while also attaining coefficients of zero for the the basis operators that are not in the model (irrelevant bases). We begin by putting together the right hand side of the Equation (28) and (29) at each time $\{\dots, t_{n-1}, t_n, t_{n+1}, \dots\}$. Let

$$\mathbf{y}_1 = \begin{bmatrix} \vdots \\ \frac{1}{\Delta t} \left(\frac{1}{\widehat{V}_{n-1}} \int_{\widehat{\Omega}_{n-1}} \widehat{C}_{n-1} dv - \frac{1}{\widehat{V}_{n-2}} \int_{\widehat{\Omega}_{n-2}} \widehat{C}_{n-2} dv \right) \\ \frac{1}{\Delta t} \left(\frac{1}{\widehat{V}_n} \int_{\widehat{\Omega}_n} \widehat{C}_n dv - \frac{1}{\widehat{V}_{n-1}} \int_{\widehat{\Omega}_{n-1}} \widehat{C}_{n-1} dv \right) \\ \frac{1}{\Delta t} \left(\frac{1}{\widehat{V}_{n+1}} \int_{\widehat{\Omega}_{n+1}} \widehat{C}_{n+1} dv - \frac{1}{\widehat{V}_n} \int_{\widehat{\Omega}_n} \widehat{C}_n dv \right) \\ \vdots \end{bmatrix} \quad (36)$$

and

$$\mathbf{y}_2 = \begin{bmatrix} \vdots \\ \frac{1}{2\Delta t} \left(\frac{1}{\widehat{V}_{n-1}} \int_{\widehat{\Omega}_{n-1}} \widehat{C}_{n-1}^2 dv - \frac{1}{\widehat{V}_{n-2}} \int_{\widehat{\Omega}_{n-2}} \widehat{C}_{n-2}^2 dv \right) - \frac{1}{\widehat{V}_{n-1}} \int_{\widehat{\Omega}_{n-1}} \widehat{C} \widehat{\chi}_1 dv \cdot \boldsymbol{\omega}_1 \\ \frac{1}{2\Delta t} \left(\frac{1}{\widehat{V}_n} \int_{\widehat{\Omega}_n} \widehat{C}_n^2 dv - \frac{1}{\widehat{V}_{n-1}} \int_{\widehat{\Omega}_{n-1}} \widehat{C}_{n-1}^2 dv \right) - \frac{1}{\widehat{V}_n} \int_{\widehat{\Omega}_n} \widehat{C} \widehat{\chi}_1 dv \cdot \boldsymbol{\omega}_1 \\ \frac{1}{2\Delta t} \left(\frac{1}{\widehat{V}_{n+1}} \int_{\widehat{\Omega}_{n+1}} \widehat{C}_{n+1}^2 dv - \frac{1}{\widehat{V}_n} \int_{\widehat{\Omega}_n} \widehat{C}_n^2 dv \right) - \frac{1}{\widehat{V}_{n+1}} \int_{\widehat{\Omega}_{n+1}} \widehat{C} \widehat{\chi}_1 dv \cdot \boldsymbol{\omega}_1 \\ \vdots \end{bmatrix} \quad (37)$$

be our two target vector. Likewise we can form the matrix, $\boldsymbol{\Xi}_1$ and $\boldsymbol{\Xi}_2$, containing all possible operator bases:

$$\boldsymbol{\Xi}_1 = \begin{bmatrix} \vdots & \vdots & \vdots & \vdots \\ \frac{1}{\widehat{V}_{n-1}} \int_{\widehat{\Omega}_{n-1}} 1 dv & \frac{1}{\widehat{V}_{n-1}} \int_{\widehat{\Omega}_{n-1}} \widehat{C}_{n-1} dv & \frac{1}{\widehat{V}_{n-1}} \int_{\widehat{\Omega}_{n-1}} \widehat{C}_{n-1}^2 dv & \dots \\ \frac{1}{\widehat{V}_n} \int_{\widehat{\Omega}_n} 1 dv & \frac{1}{\widehat{V}_n} \int_{\widehat{\Omega}_n} \widehat{C}_n dv & \frac{1}{\widehat{V}_n} \int_{\widehat{\Omega}_n} \widehat{C}_n^2 dv & \dots \\ \frac{1}{\widehat{V}_{n+1}} \int_{\widehat{\Omega}_{n+1}} 1 dv & \frac{1}{\widehat{V}_{n+1}} \int_{\widehat{\Omega}_{n+1}} \widehat{C}_{n+1} dv & \frac{1}{\widehat{V}_{n+1}} \int_{\widehat{\Omega}_{n+1}} \widehat{C}_{n+1}^2 dv & \dots \\ \vdots & \vdots & \vdots & \vdots \end{bmatrix} \quad (38)$$

$$\boldsymbol{\Xi}_2 = \begin{bmatrix} \vdots & \vdots & \vdots & \vdots \\ \frac{1}{\widehat{V}_{n-1}} \int_{\widehat{\Omega}_{n-1}} \nabla \widehat{C}_{n-1} \cdot \nabla \widehat{C}_{n-1} dv & \frac{1}{\widehat{V}_{n-1}} \int_{\widehat{\Omega}_{n-1}} \widehat{C}_{n-1} \nabla \widehat{C}_{n-1} \cdot \nabla \widehat{C}_{n-1} dv & \frac{1}{\widehat{V}_{n-1}} \int_{\widehat{\Omega}_{n-1}} \nabla^2 \widehat{C}_{n-1} \nabla^2 \widehat{C}_{n-1} dv & \dots \\ \frac{1}{\widehat{V}_n} \int_{\widehat{\Omega}_n} \nabla \widehat{C}_n \cdot \nabla \widehat{C}_n dv & \frac{1}{\widehat{V}_n} \int_{\widehat{\Omega}_n} \widehat{C}_n \nabla \widehat{C}_n \cdot \nabla \widehat{C}_n dv & \frac{1}{\widehat{V}_n} \int_{\widehat{\Omega}_n} \nabla^2 \widehat{C}_n \nabla^2 \widehat{C}_n dv & \dots \\ \frac{1}{\widehat{V}_{n+1}} \int_{\widehat{\Omega}_{n+1}} \nabla \widehat{C}_{n+1} \cdot \nabla \widehat{C}_{n+1} dv & \frac{1}{\widehat{V}_{n+1}} \int_{\widehat{\Omega}_{n+1}} \widehat{C}_{n+1} \nabla \widehat{C}_{n+1} \cdot \nabla \widehat{C}_{n+1} dv & \frac{1}{\widehat{V}_{n+1}} \int_{\widehat{\Omega}_{n+1}} \nabla^2 \widehat{C}_{n+1} \nabla^2 \widehat{C}_{n+1} dv & \dots \\ \vdots & \vdots & \vdots & \vdots \end{bmatrix} \quad (39)$$

Then Equations (28) and (29) can be expressed as

$$\text{Stage 1: } \quad \mathbf{y}_1 = \boldsymbol{\Xi}_1 \boldsymbol{\omega}_1 \quad (40)$$

and

$$\text{Stage 2: } \mathbf{y}_2(\boldsymbol{\omega}_1) = \boldsymbol{\Xi}_2 \boldsymbol{\omega}_2 \quad (41)$$

Equations (40-41) immediately deliver the two-stage algorithm of Variational System Identification, first for the coefficient vector $\boldsymbol{\omega}_1$ first, and then for $\boldsymbol{\omega}_2$ given the estimation of $\boldsymbol{\omega}_1$. Thus splitting the process into two stages also alleviates the curse of dimensionality as a smaller number of operators needs to be considered at each stage for parsimonious identification.

If Equation (40) and (41) are directly solved for $\boldsymbol{\omega}_1$ and $\boldsymbol{\omega}_2$ as ordinary least squares problems, the analytic solution is

$$\boldsymbol{\omega}_1 = (\boldsymbol{\Xi}_1^T \boldsymbol{\Xi}_1)^{-1} \boldsymbol{\Xi}_1^T \mathbf{y}_1 \quad (42)$$

$$\boldsymbol{\omega}_2 = (\boldsymbol{\Xi}_2^T \boldsymbol{\Xi}_2)^{-1} \boldsymbol{\Xi}_2^T \mathbf{y}_2 \quad (43)$$

The least squares formulations can also be interpreted as an optimization problem with the loss functions

$$l_1 = (\mathbf{y}_1 - \boldsymbol{\Xi}_1 \boldsymbol{\omega}_1)^T (\mathbf{y}_1 - \boldsymbol{\Xi}_1 \boldsymbol{\omega}_1) \quad (44)$$

$$l_2 = (\mathbf{y}_2 - \boldsymbol{\Xi}_2 \boldsymbol{\omega}_2)^T (\mathbf{y}_2 - \boldsymbol{\Xi}_2 \boldsymbol{\omega}_2) \quad (45)$$

The system identification problem can then be viewed as finding $\boldsymbol{\omega}$ that minimizes the loss:

$$\boldsymbol{\omega}_1 = \arg \min_{\tilde{\boldsymbol{\omega}}_1} l_1(\tilde{\boldsymbol{\omega}}_1) \quad (46)$$

$$\boldsymbol{\omega}_2 = \arg \min_{\tilde{\boldsymbol{\omega}}_2} l_2(\tilde{\boldsymbol{\omega}}_2) \quad (47)$$

To have more robustness in dealing with noise and outliers, we use ridge regression to induce regularization. The optimization problem Equation (46) and Equation (47) are updated with additional penalty terms

$$\boldsymbol{\omega}_1 = \arg \min_{\tilde{\boldsymbol{\omega}}_1} \{l_1(\boldsymbol{\omega}_1) + \lambda_1 \|\boldsymbol{\omega}_1\|^2\} \quad (48)$$

$$\boldsymbol{\omega}_2 = \arg \min_{\tilde{\boldsymbol{\omega}}_2} \{l_2(\boldsymbol{\omega}_2) + \lambda_2 \|\boldsymbol{\omega}_2\|^2\} \quad (49)$$

$$(50)$$

where λ_1 and λ_2 are hyper-parameters.

However, performing a standard ridge regression will result in a solution of $\boldsymbol{\omega}$ with nonzero contributions in all components of this vector. Such a solution of the system identification will lose parsimony in failing to sharply delineate the relevant bases.

2.4.1 Stepwise regression

In this work, we use backward model selection by stepwise regression [31], which, as we demonstrate, delivers parsimonious results. The algorithm is summarized below.

Algorithm for Model selection by Stepwise regression:

Step 0: Establish target vector \mathbf{y} and matrix of bases, Ξ .

Step 1: Solve ω^i in the linear regression problem, Equation (40) and Equation (41), using ridge regression. Calculate the loss function at this iteration, l^i .

Step 2: Eliminate basis terms in matrix Ξ by deleting their columns, using the criterion to be introduced below. Set to zero the corresponding components of ω^i . GOTO Step 1. Note that at this stage the loss function remains small ($l^i \sim l^{i-1}$), and the solution may be overfitted.

Step 3: The algorithm stops if the pre-specified criterion does not allow us to eliminate any more basis terms. Beyond this, the loss function increases dramatically for any further reduction.

There are several choices for the criterion for eliminating basis terms. Here, we explore a widely used statistical criterion called the F -test, also used by us previously [26]. The significance of the change between model at iteration i and $i - 1$ is evaluated by:

$$F = \frac{\left(\frac{l^i - l^{i-1}}{p^{i-1} - p^i} \right)}{\frac{l^{i-1}}{n - p^{i-1}}} \quad (51)$$

where p^i is the number of bases at iteration i and n is the total number of bases. Model selection is performed by following algorithm:

model selection by F -test:

Step 1:

Tentatively eliminate the basis corresponding to coefficients in ω^i which are smaller than the pre-defined threshold. Evaluate the F value followed by ridge regression on the reduced bases set.

Step 2:

IF $F < \alpha$

THEN formally eliminate these bases in matrix Ξ , by deleting the corresponding columns. GOTO Step 1.

ELSE GOTO Step 1, and choose another basis.

In this work we defined the threshold to be:

$$\text{threshold}^i = \omega_{\text{smallest}}^i + \epsilon \quad (52)$$

where $\omega_{\text{smallest}}^i$ is the smallest value in ω^i , and ϵ is a small tolerance. Note the penalty coefficients in ridge regression, λ_1 and λ_2 , are chosen to lie in the range $[10^{-10}, 10^{-1}]$ by Leave-One-Out cross-validation at each iteration. The hyperparameter α is chosen to lie in the range $[1, 10]$, by five-fold cross validation.

We have summarized the step-wise algorithm in Figure 2.

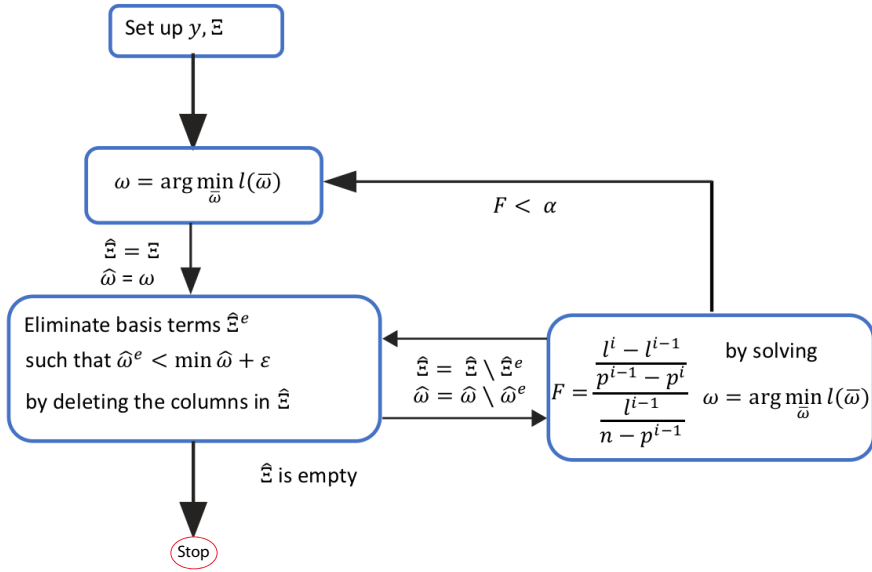


Figure 2: Schematic of the complete algorithm for stepwise regression.

Note the method of moments yields only one “data point”, i.e. one row in the linear system (40-41), given a snapshot at one time step and considering one type of moment. Consequently this method needs a large data set to delineate the relevant bases. However, we can leverage the data at steady state to identify the only the spatial operators first, followed by inference of the dynamics via the method of moments. This is discussed in the following section.

2.5 Identification of basis operators via the two stage method with data at steady state

We point out first that data with high spatial resolution at steady state is typically obtained from modern microscopy methods In fact the data satisfying the steady state equation:

$$\chi \cdot \omega = 0, \quad (53)$$

already provide rich information about the spatial operators in the system. By choosing a nontrivial, χ_1 , to be the target vector and writing the equation as:

$$-\chi_1 = \frac{1}{\omega_1} \tilde{\chi} \cdot \tilde{\omega}, \quad (54)$$

where $\tilde{\chi} = \chi \setminus \{\chi_1\}$ and $\tilde{\omega} = \omega \setminus \{\omega_1\}$. We are able to identify the coefficients, $\tilde{\omega}$, up to a scaling constant, ω_1 , using the data at steady state by Variational System Identification [26]. Thereafter, there remains only one unknown in the governing equations:

$$\frac{\partial C}{\partial t} - \omega_1(\chi \cdot \omega) = 0, \quad (55)$$

which then can be identified using the data at early times using the Method of Moments detailed above.

Note if the operator, χ_1 , is inactive (i.e., its prefactor $\omega_1 = 0$), then Equation (54) is not valid. Given the data, the system identification may not be able to yield sparse sparse results in $\tilde{\chi}$, and the “false” results could be detected by inconsistencies in the system identification; ie, the regression is fitting the noise in the data and amplifying these false signals. This is elaborated with examples in Section 3.5, and proves to be a powerful feature in favor of robustness and consistency of the combined, Variational System Identification at steady state followed by the Method of Moments approach.

3 Examples

We now turn to using the framework detailed in the preceding section to identify the parabolic PDEs that govern patterning. Instead of directly applying our algorithms to data from physical experiments, we test our methods on identifying PDEs from data obtained through high-fidelity, direct numerical simulations (DNS).

We consider test cases with the following two data-generating models, with their true coefficients summarized in Table 1:

Model 1:

$$\frac{\partial C_1}{\partial t} = D_1 \nabla^2 C_1 + R_{10} + R_{11} C_1 + R_{13} C_1^2 C_2 \quad (56)$$

$$\frac{\partial C_2}{\partial t} = D_2 \nabla^2 C_2 + R_{20} + R_{21} C_1^2 C_2 \quad (57)$$

$$\text{with } \nabla C_1 \cdot \mathbf{n} = 0; \quad \nabla C_2 \cdot \mathbf{n} = 0 \text{ on } \Gamma \quad (58)$$

where Γ is the domain boundary. Model 1 represents the coupled diffusion-reaction equations for two species following Schnakenberg kinetics [32], but with different boundary conditions. For an

activator-inhibitor species pair, these equations use auto-inhibition with cross-activation of a short range species, and auto-activation with cross-inhibition of a long range species to form so-called Turing patterns [4].

Model 2:

$$\frac{\partial C_1}{\partial t} = \nabla \cdot (M_1 \nabla \mu_1) \quad (59)$$

$$\frac{\partial C_2}{\partial t} = \nabla \cdot (M_2 \nabla \mu_2) \quad (60)$$

$$\mu_1 = \frac{\partial g}{\partial C_1} - k_1 \nabla^2 C_1 \quad (61)$$

$$\mu_2 = \frac{\partial g}{\partial C_2} - k_2 \nabla^2 C_2 \quad (62)$$

$$\text{with } \nabla \mu_1 \cdot \mathbf{n} = 0; \nabla C_1 \cdot \mathbf{n} = 0 \text{ on } \Gamma \quad (63)$$

$$\nabla \mu_2 \cdot \mathbf{n} = 0; \nabla C_2 \cdot \mathbf{n} = 0 \text{ on } \Gamma \quad (64)$$

where g is a non-convex, “homogeneous” free energy density function, whose form has been chosen from [13]:

$$g(C_1, C_2) = \frac{3d}{2s^4} ((2C_1 - 1)^2 + (2C_2 - 1)^2)^2 + \frac{d}{s^3} (2C_2 - 1) ((2C_2 - 1)^2 - 3(2C_1 - 1)^2) - \frac{3d}{2s^2} ((2C_1 - 1)^2 + (2C_2 - 1)^2). \quad (65)$$

Model 2 is a two fields Cahn-Hilliard system with the well-known fourth-order term in the concentration, C_1 and C_2 . The three-well non-convex free energy density function (See Figure 3), $g(C_1, C_2)$, drives segregation of the system into two distinct types. We have previously used this system to make connections with cell segregation in developmental biology [13]. The diffusion-reaction and Cahn-Hilliard equations are widely used in biological pattern generation, as discussed in the Introduction. The Cahn-Hilliard equation [14] also occupies a central role in the materials physics literature for modelling phase transformations developing from a uniform concentration field in the presence of an instability.

| D_1 | D_2 | R_{10} | R_{11} | R_{13} | R_{20} | R_{21} | M_1 | M_2 | k_1 | k_2 | d | s |
|-------|-------|----------|----------|----------|----------|----------|-------|-------|-------|-------|-----|-----|
| 1 | 40 | 0.1 | -1 | 1 | 0.9 | -1 | 0.1 | 0.1 | 10 | 10 | 0.4 | 0.7 |

Table 1: parameters used in the simulations.

Substituting the parameter values from Table 1, we present the weak form of each model:

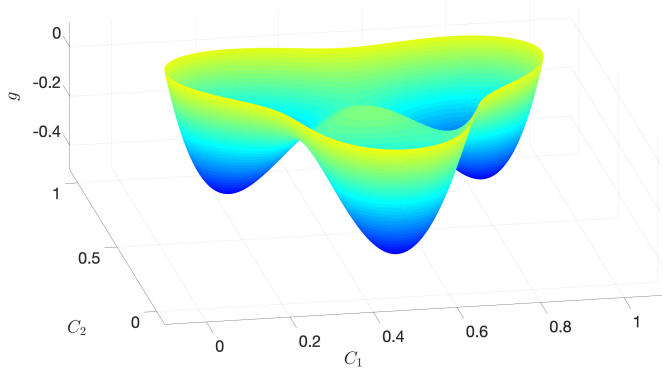


Figure 3: The three wells non-convex tissue energy density function.

Model 1:

$$\int_{\Omega} w_1 \frac{\partial C_1}{\partial t} dv = \int_{\Omega} -1 \nabla w_1 \cdot \nabla C_1 dv + \int_{\Omega} w_1 (0.1 - C_1 + 1C_1^2 C_2) dv \quad (66)$$

$$\int_{\Omega} w_2 \frac{\partial C_2}{\partial t} dv = \int_{\Omega} -40 \nabla w_2 \cdot \nabla C_2 dv + \int_{\Omega} w_2 (0.9 - 1C_1^2 C_2) dv \quad (67)$$

Model 2:

$$\begin{aligned} \int_{\Omega} w_1 \frac{\partial C_1}{\partial t} dv &= \int_{\Omega} \nabla w_1 \cdot (-17.8126 + 47.98C_1 + 21.591C_2 - 47.98C_1^2 - 15.9933C_2^2) \nabla C_1 dv \\ &+ \int_{\Omega} \nabla w_1 \cdot (-10.7955 + 21.591C_1 + 15.9933C_2 - 31.9867C_1C_2) \nabla C_2 dv \\ &+ \int_{\Omega} -1 \nabla^2 w_1 \nabla^2 C_1 dv \end{aligned} \quad (68)$$

$$\begin{aligned} \int_{\Omega} w_2 \frac{\partial C_2}{\partial t} dv &= \int_{\Omega} \nabla w_2 \cdot (-10.7955 + 21.591C_1 + 15.9933C_2 - 31.9867C_1C_2) \nabla C_1 dv \\ &+ \int_{\Omega} \nabla w_2 \cdot (-12.2149 + 15.9933C_1 + 42.3823C_2 - 15.9933C_1^2 - 47.98C_2^2) \nabla C_2 dv \\ &+ \int_{\Omega} -1 \nabla^2 w_2 \nabla^2 C_2 dv \end{aligned} \quad (69)$$

3.1 Data preparation

All computations have been implemented in the `mechanoChemIGA` framework, a library for modeling mechano-chemical problems using isogeometric analytics, available at <https://github.com/>

mechanoChem/mechanoChem. The IBVPs presented here are two-dimensional. The initial conditions for all simulations are

$$C_1 = 0.5 + \delta$$

$$C_2 = 0.5 + \delta$$

where $\delta \in [-0.01, 0.01]$ is a random real number.

To mimic the experimental data that are collected from multiple samples, we run each model 30 times, with the small perturbation, δ , re-generated for every case (upper plots in Figure 4). The patterns generated from different initial conditions are different but statistically similar (see lower plots in Figure 4). We collected the data at 30 time steps and at each time step the data are collected from different forward simulations.

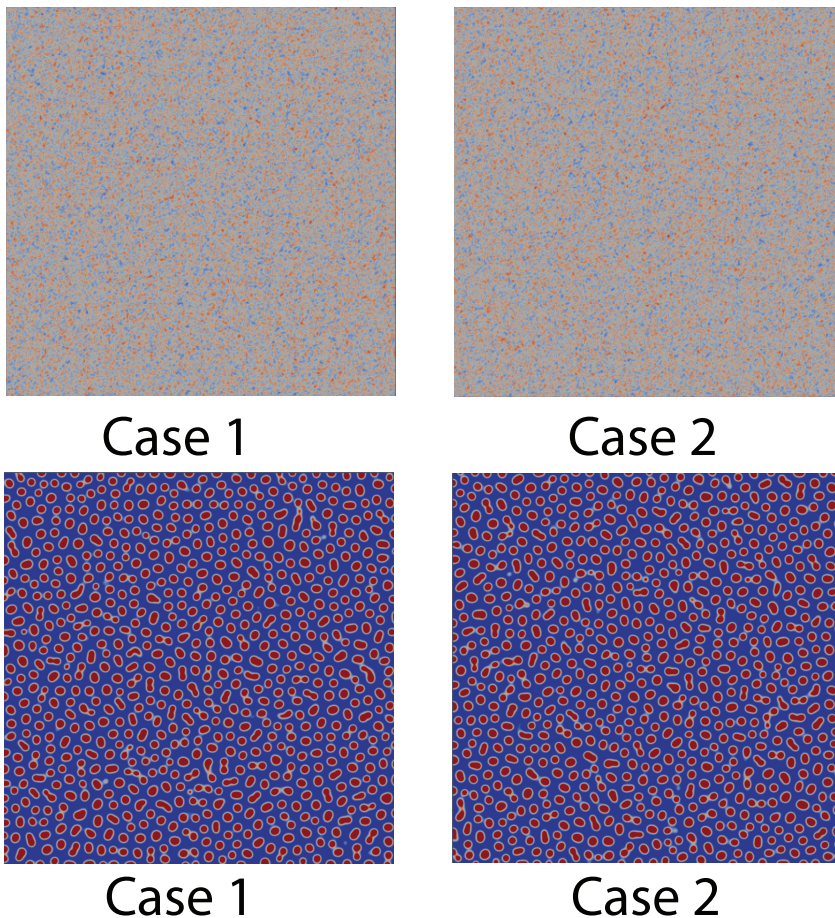


Figure 4: Upper plots: Concentration at $t = 0$ of two cases representing distinct experimental samples. The perturbation is re-generated for every case. Lower plots: Concentration at $t = 20$. The Turing patterns generated from different initial conditions are statistically similar.

The experimental data may also be noisy and at lower fidelity, having been collected at fewer spatial positions. To mimic experimental data, We superpose noise with a Gaussian distribution having zero mean and standard deviation σ , on the collected (C_1, C_2) . We first collect the DNS data, from all four models, on DOFs corresponding to the 400×400 mesh, which was used for the forward computations. Data from the same forward computations were then collected on the DOFs corresponding to the smaller 200×200 , 100×100 and 50×50 meshes. Having the clean and noisy data at different fidelity from different samples, we generate 38 candidate bases in addition to the time derivative terms, summarized in Table 2.

Table 2: Candidate basis for model selection. Asterisks, (*) in the left column represent algebraic operators on C_1 and C_2 . Note the weighting function w will be replaced by 1 or C .

| type of basis | basis in weak form |
|-------------------------|---|
| $\nabla(*\nabla C_1)$ | $\int_{\Omega} \nabla w \nabla C_1 dv \quad \int_{\Omega} \nabla w C_1 \nabla C_1 dv \quad \int_{\Omega} \nabla w \nabla C_2 dv$ $\int_{\Omega} \nabla w C_1^2 \nabla C_1 dv \quad \int_{\Omega} \nabla w C_1 C_2 \nabla C_1 dv \quad \int_{\Omega} \nabla w C_2^2 \nabla C_1 dv$ $\int_{\Omega} \nabla w C_1^3 \nabla C_1 dv \quad \int_{\Omega} \nabla w C_1^2 C_2 \nabla C_1 dv \quad \int_{\Omega} \nabla w C_1 C_2^2 \nabla C_1 dv \quad \int_{\Omega} \nabla w C_2^3 \nabla C_1 dv$ |
| $\nabla(*\nabla C_2)$ | $\int_{\Omega} \nabla w \nabla C_2 dv \quad \int_{\Omega} \nabla w C_1 \nabla C_2 dv \quad \int_{\Omega} \nabla w \nabla C_2 dv$ $\int_{\Omega} \nabla w C_1^2 \nabla C_2 dv \quad \int_{\Omega} \nabla w C_1 C_2 \nabla C_2 dv \quad \int_{\Omega} \nabla w C_2^2 \nabla C_2 dv$ $\int_{\Omega} \nabla w C_1^3 \nabla C_2 dv \quad \int_{\Omega} \nabla w C_1^2 C_2 \nabla C_2 dv \quad \int_{\Omega} \nabla w C_1 C_2^2 \nabla C_2 dv \quad \int_{\Omega} \nabla w C_2^3 \nabla C_2 dv$ |
| $\nabla^2(*\nabla^2 C)$ | $\int_{\Omega} \nabla^2 w \nabla^2 C_1 dv \quad \int_{\Omega} \nabla^2 w C_1 \nabla^2 C_1 dv \quad \int_{\Omega} \nabla^2 w \nabla^2 C_2 dv \quad \int_{\Omega} \nabla^2 w C_2 \nabla^2 C_2 dv$ |
| non-gradient | $-\int_{\Omega} w dv \quad -\int_{\Omega} w C_1 dv \quad -\int_{\Omega} w C_2 dv$ $-\int_{\Omega} w C_1^2 dv \quad -\int_{\Omega} w C_1 C_2 dv \quad -\int_{\Omega} w C_2^2 dv$ $-\int_{\Omega} w C_1^3 dv \quad -\int_{\Omega} w C_1^2 C_2 dv \quad -\int_{\Omega} w C_1 C_2^2 dv \quad -\int_{\Omega} w C_2^3 dv$ |

3.2 Statistical similarity in the data of pattern forming physics

Before identifying the governing equations, we examine the synthetic data, and verify the two key assumptions made in Section 2.2. Figures 5 and 6 show the first and second moments of C_1 and C_2 evaluated using data at different sizes of snapshots from different simulations. The random perturbation affects the local distribution of C_1 and C_2 ; however, with increasing size of snapshots the statistical similarity become dominant. Consequently evaluated moments using data from snapshots converge to the moments using full field data (corresponding to Key Assumption 1), and evaluated moments using data from all 30 different simulations converge to to the moments using full field data (corresponding to Key Assumption 2).

The statistical similarity is due to the random distribution of features/particles in the pattern forming physics. The patterns formed by the diffusion-reaction system reach steady state as shown in the left plot in Figure 7. We can calculate the ratio of particle numbers within the different sized snapshots to the total particle number. Since the particles are randomly distributed in the

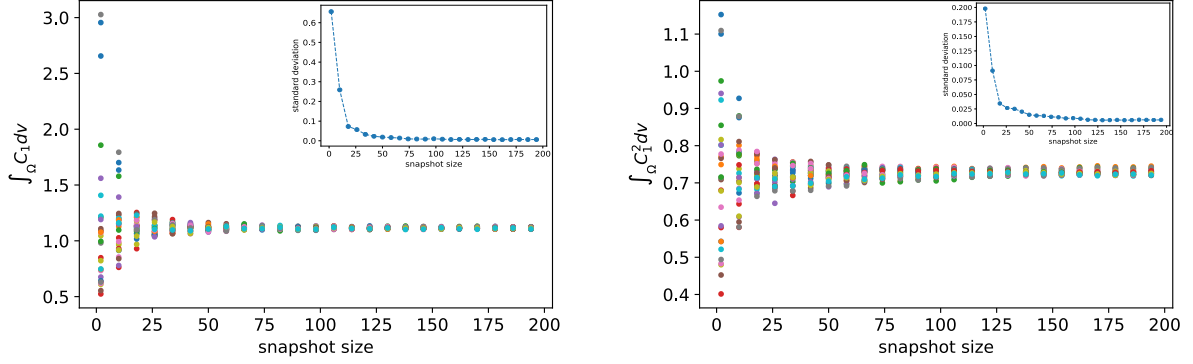


Figure 5: The first (left plot) and second moment (right plot) of C_1 evaluated using data from 30 different simulations, marked by different colors, with different snapshot size. The embedded subplot shows the decreasing standard deviation of moments, evaluated using data from different samples, with increasing snapshot size.

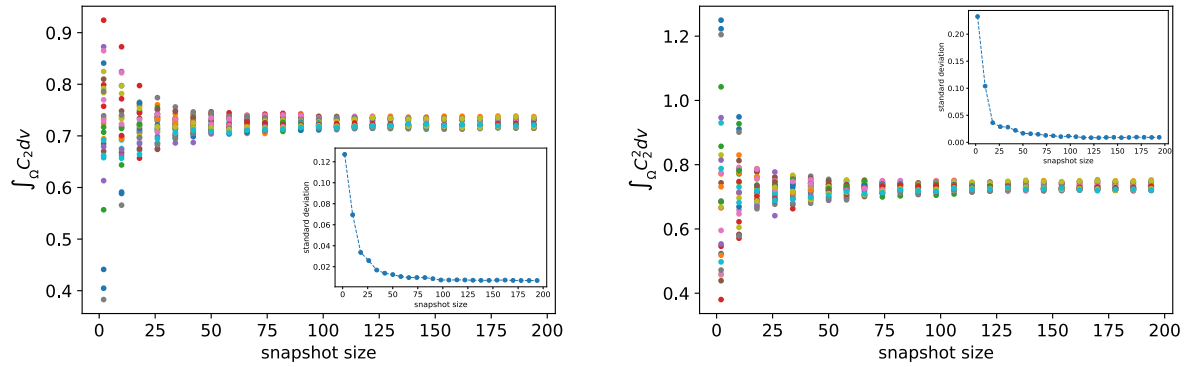


Figure 6: The first (left plot) and second moment (right plot) of C_2 evaluated using data from 30 different simulations, marked by different colors, with different snapshot size. The embedded subplot shows the decreasing standard deviation of moments, evaluated using data from different samples, with increasing snapshot size.

domain, the ratio increases quadratically with increasing snapshot size. In the following examples we test our methods using snapshot with sizes of 50, 100, 200, 300 and 400, which contain about 1.56%, 6.25%, 25%, 56.25% and 100% of the total number of particles, respectively. Note that at early times the particle distribution is affected by the initial perturbation and also may not be fully developed.

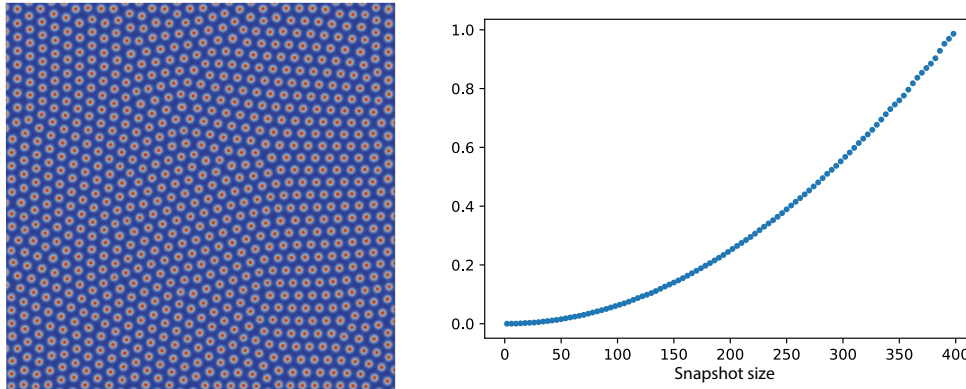


Figure 7: The left plot shows the C_1 concentration at steady state. The right plot shows the ratio of number of particles within snapshots to the total number of particle in the whole domain. The area of a snapshot is the square of its size, and thus the fraction is a quadratic function around $\frac{\text{size}^2}{400^2}$

3.3 System identification with incomplete data from different samples without noise

The approximation of time derivatives needs data from two time steps which are collected from different simulations. Figure 8 shows the time derivatives constructed using data collected from different sizes of snapshots at each time step. Smaller snapshots yield very noisy approximation especially at later times when the dynamic system is close to steady state and time variations are minimal, thus not aiding the identification of dynamic operators. The basis operators shown in Figure 9, which are constructed only using data at current times, are less noisy compared to the time derivatives. The poor representations sabotage the system identification, as we will discuss below.

In Stage 1 we successfully determined the non-gradient dependent operators in the governing equation for C_1 shown in Figure 10. The loss remains small until it converges. The data collected from larger snapshots yields lower losses, which also increase more dramatically compared to results using smaller snapshots, when relevant operators are eliminated by trial in the stepwise regression process. In Stage 2 we successfully determined the one gradient dependent operator in the governing

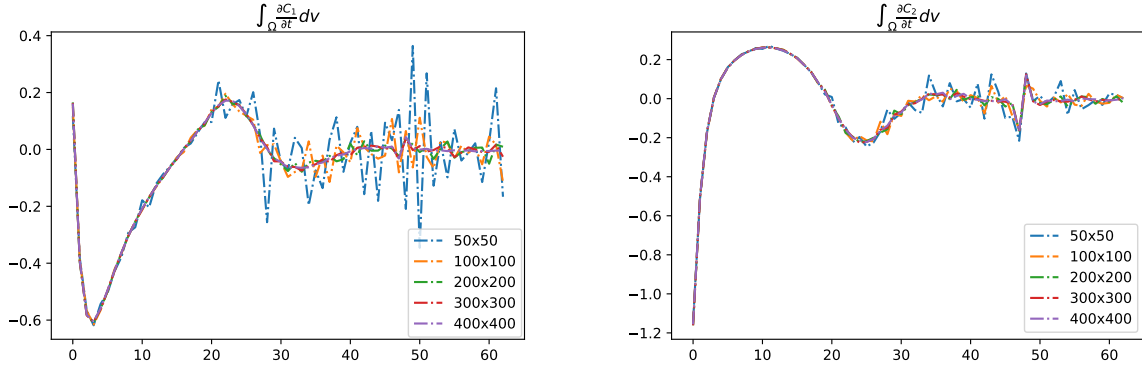


Figure 8: Time evolution of $\int_{\Omega} \frac{\partial C_1}{\partial t} dv$ and $\int_{\Omega} \frac{\partial C_2}{\partial t} dv$. The constructed time derivatives is noisy using small snapshot at time close to steady state.

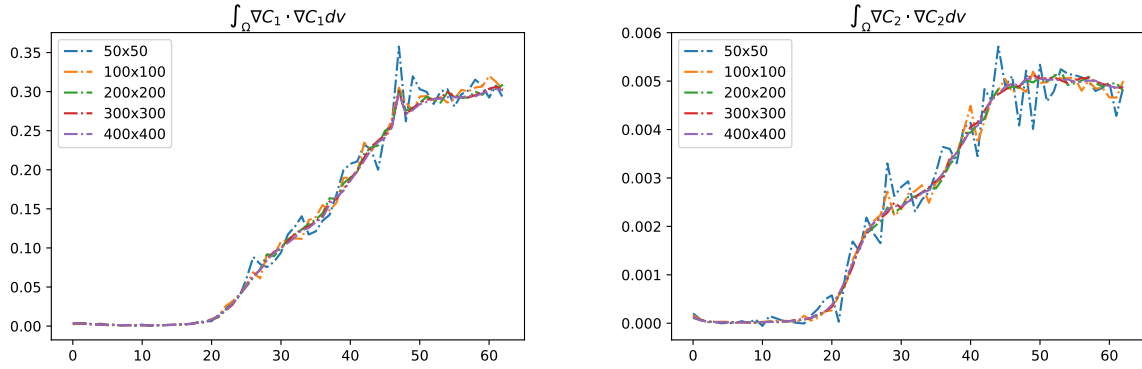


Figure 9: Time evolution of basis operator $\int_{\Omega} \nabla C_1 \cdot \nabla C_1 dv$ and $\int_{\Omega} \nabla C_2 \cdot \nabla C_2 dv$ are less noisy than time derivatives in Figure 8.

equation shown in Figure 11. We notice that in Stage 1 the “moderately” increasing loss function using data collected from small snapshots (50×50 mesh) needs a relative small F -test criterion, ($\alpha \sim 1$). to keep the the rest of the operators. However, in Stage 2 the loss functions increase by half order in the last few iterations using data collected from 100×100 and 50×50 mesh, thus needing a bigger F -test criterion, ($\alpha \sim 10$), to eliminate the corresponding operators. These “slightly” increasing losses present a challenge to the stepwise regression procedure for selection of a proper α for the F -test. Thus proper cross validation is needed to choose the best α by balancing model complexity and accuracy.

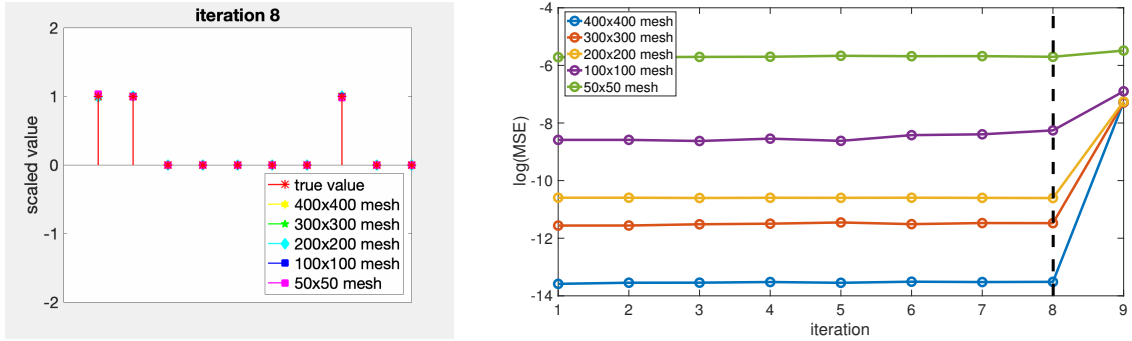


Figure 10: Inferred operators for C_1 (left panel) at the first stage , and the loss (right panel) at each iteration using data generated from Model 1. The identified coefficients of relevant terms are scaled by their true values. The algorithm converged at iteration 8 as the loss increases dramatically if any more operators are eliminated.

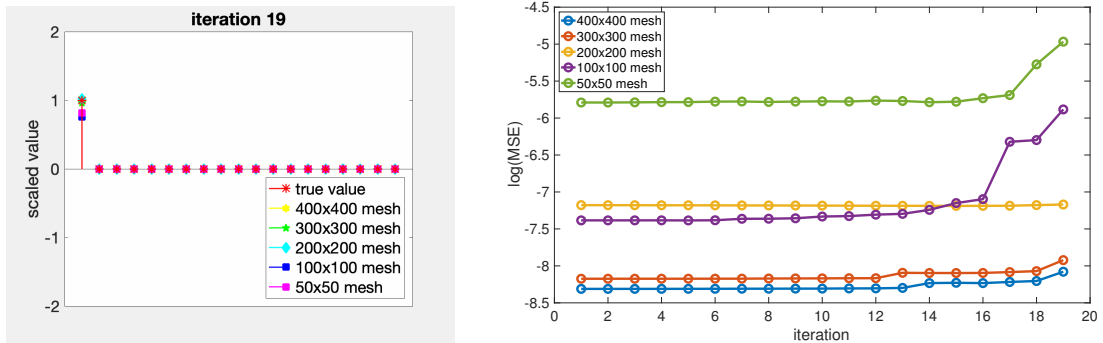


Figure 11: Inferred operators for C_1 (left panel) at the second stage, and the loss (right panel) at each iteration using data generated from Model 1. The identified coefficients of relevant terms are scaled by their true values. The algorithm converged at iteration 19 when only one operator left.

Figure 12 shows that the non-gradient dependent operators in the governing equation for C_2 are correctly identified. Also, all the loss functions increase dramatically if any more operators

are eliminated after converging. This is because the time derivative term (right plot in Figure 8) and the non-gradient dependent operators are well approximated even using data collected from small snapshots. However the the gradient dependent operator is identified wrongly using small snapshots, (100×100 and 50×50 mesh), as shown in Figure 13. This is because the the gradient dependent operator for C_2 (See Figure 9) is poorly approximated using the data collected from the smaller snapshots.

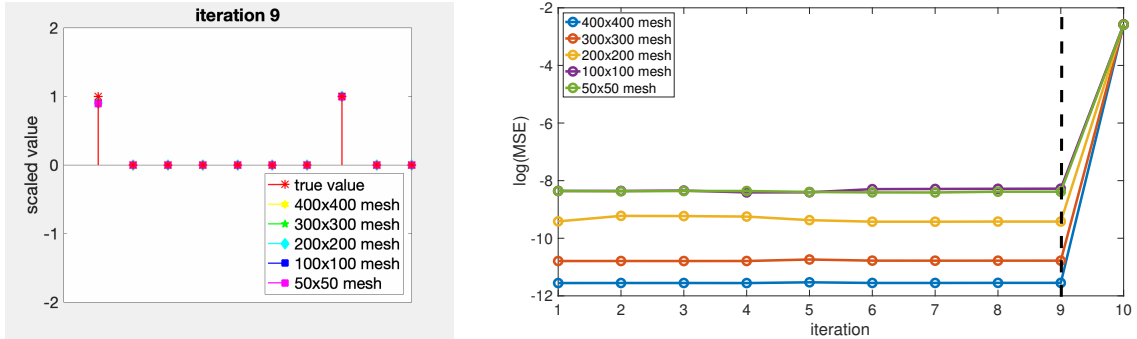


Figure 12: Inferred operators for C_2 (left panel) at the first stage, and the loss (right panel) at each iteration using data generated from Model 1. The identified coefficients of relevant terms are scaled by their true values. The algorithm converged at iteration 9 as the loss increases dramatically if any more operators are eliminated.

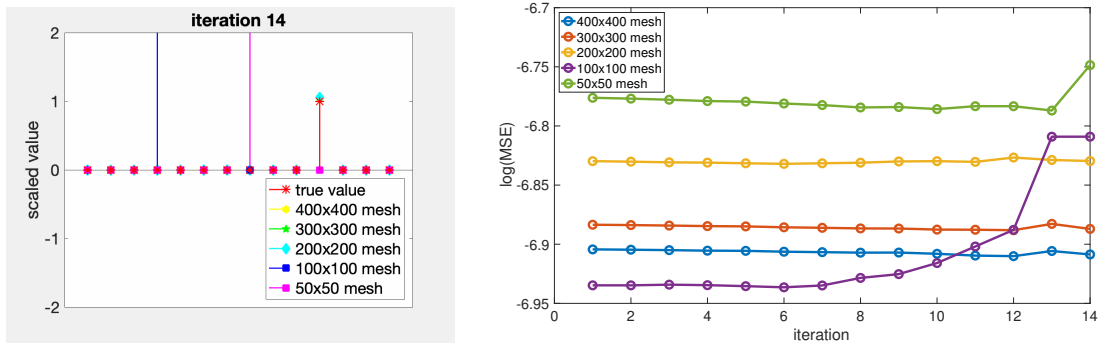


Figure 13: Inferred operators for C_2 (left panel) at the second stage, and the loss (right panel) at each iteration using data generated from Model 1. The identified coefficients of relevant terms are scaled by their true values. The algorithm converges at iteration 19 when only one operator remains.

3.4 System identification with incomplete data from different samples with noise

We superimpose noise with $\sigma = 0.01$ for data generated from Models 1. The noise on C_1 and C_2 will be amplified in the time derivative and spatial gradients. As shown in Figure 14, the noise washed out the true value of spatial gradient operators $\nabla^2 C_1$. The high noise in the constructed operators may fail the system identification using the VSI approach[26]. However due to the character of integration, the noise cancels out in the form of moments, and the constructed operators here, (after choosing a specific weighting function) is insensitive to noise. Similar to the results using noise-

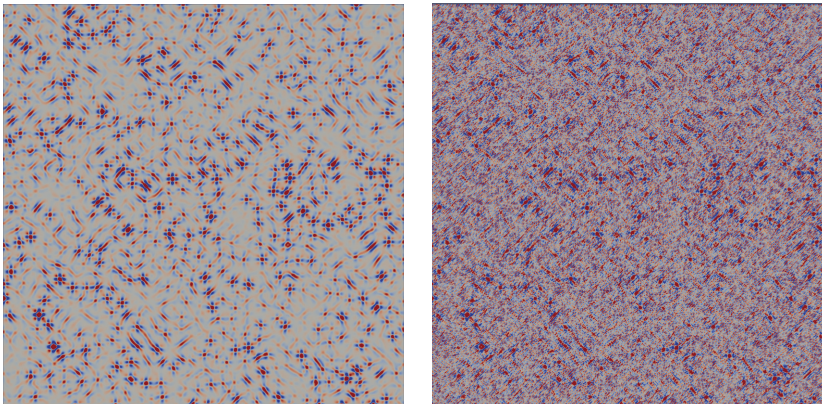


Figure 14: Noise-free (left) and noisy (right) field $\nabla^2 C_1$.

free data, for the governing equation of C_1 , all non-gradient dependent operators are successfully identified at Stage 1 using noisy data shown in Figure 15, and the one gradient dependent operator is also identified afterwards as shown in Figure 16. Though the loss function is in general higher than that using noise-free data, and the error in the coefficients of the identified operators is also higher. Likewise for the governing equation of C_2 , all non-gradient dependent operators are successfully identified at Stage 1 using noisy data shown in Figure 17, while the gradient dependent operator is identified wrongly using small snapshots, (100×100 and 50×50 mesh), as shown in Figure 18.

3.5 System identification via two stage method with data at steady state

The steady state form of Model 1 is:

$$D_1 \nabla^2 C_1 + R_{10} + R_{11} C_1 + R_{13} C_1^2 C_2 = 0 \quad (70)$$

$$D_2 \nabla^2 C_2 + R_{20} + R_{21} C_1^2 C_2 = 0 \quad (71)$$

The pattern formed by diffusion-reaction systems attains steady state as shown in the left plot of Figure 7. Given the data, available for the full field or snapshots, we could identify the steady

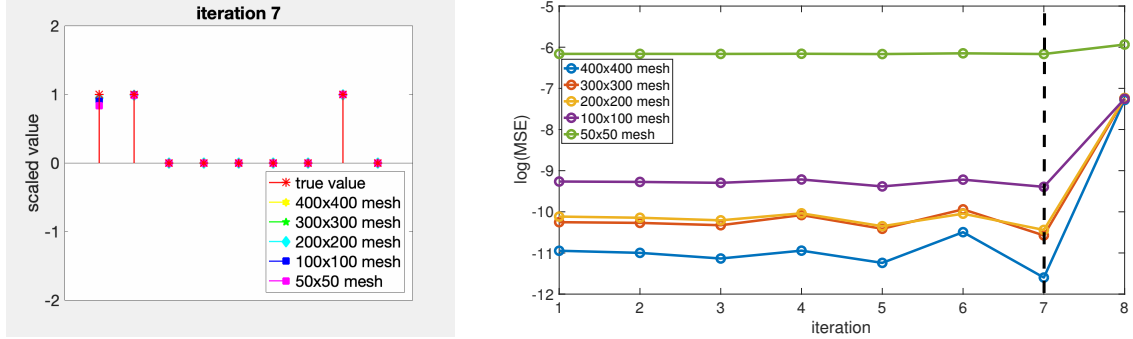


Figure 15: Inferred operators for C_1 (left panel) at the first stage, and the loss (right panel) at each iteration using data generated from Model 1 using noisy data ($\sigma = 0.01$). The identified coefficients of relevant terms are scaled by their true values. The algorithm converged at iteration 7 as the loss increases dramatically if any more operators are eliminated.

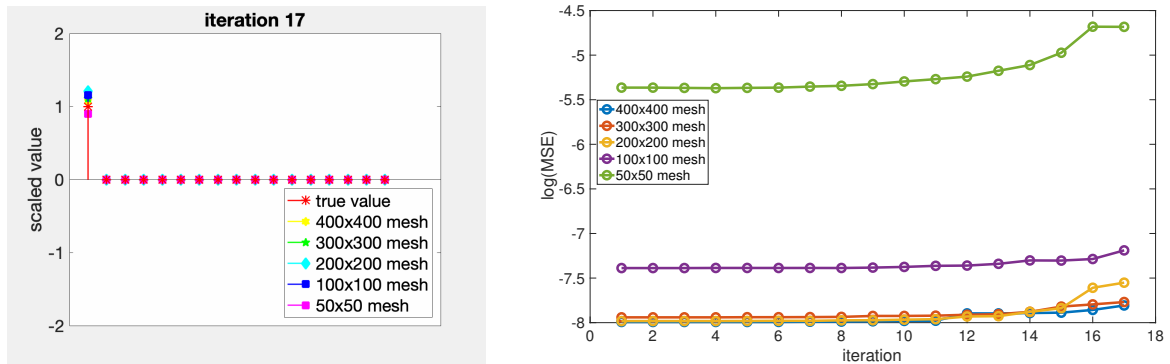


Figure 16: Inferred operators for C_1 (left panel) at the second stage, and the loss (right panel) at each iteration using data generated from Model 1 using noisy data ($\sigma = 0.01$). The identified coefficients of relevant terms are scaled by their true values. The algorithm converged at iteration 17 when only one operator left.

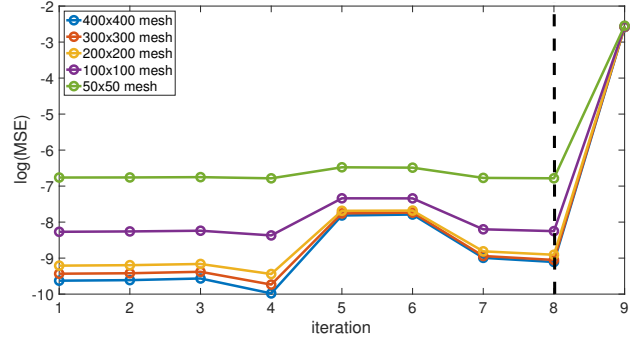
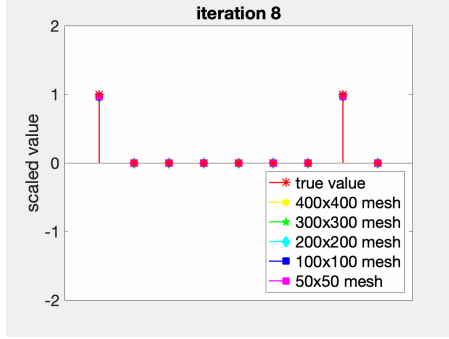


Figure 17: Inferred operators for C_2 (left panel) at the first stage, and the loss (right panel) at each iteration using data generated from Model 1 using noisy data ($\sigma = 0.01$). The identified coefficients of relevant terms are scaled by their true values. The algorithm converges at iteration 8 as the loss increases dramatically if any more operators are eliminated.

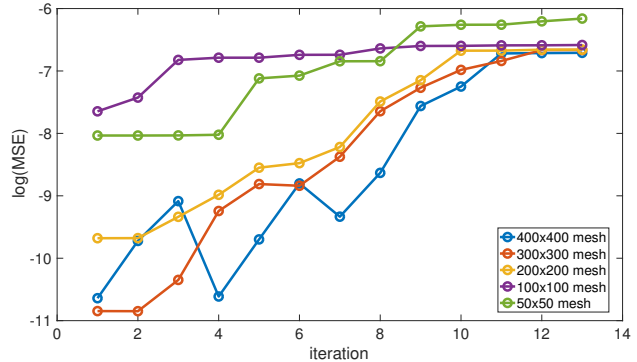
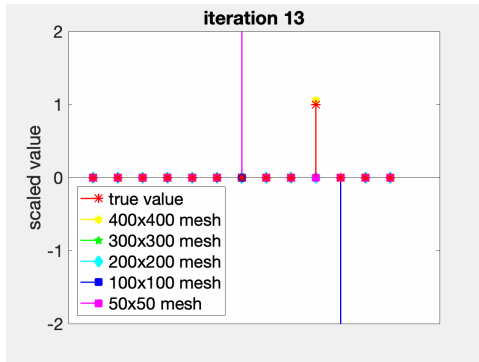


Figure 18: Inferred operators for C_1 (left panel) at the second stage, and the loss (right panel) at each iteration using data generated from Model 1 using noisy data ($\sigma = 0.01$). The identified coefficients of relevant terms are scaled by their true values. The algorithm converged at iteration 17 with only one operator remaining.

state governing equation using the Variational System Identification method discussed in Section 2.5. However without prior knowledge, we lack confidence in choosing the relevant operator to be the target vector, i.e. the left hand side in Equation (54). Choosing the irrelevant operators are more likely to yield “dense” results. But more importantly, the identified results from two different irrelevant operators are rarely, if not never, consistent. As shown in Figure 19, Choosing two different operators, $\int_{\Omega} \nabla w \cdot C_1 \nabla C_1 dv$ and $\int_{\Omega} \nabla w \cdot C_2 \nabla C_1 dv$, to be the target vector, the identified results are completely different. Also the identified operators with $\int_{\Omega} \nabla w \cdot C_1 \nabla C_1 dv$ as target vector contains $\int_{\Omega} \nabla w \cdot C_2 \nabla C_1 dv$ but not vice versa. This is because the identified results are not governed by the physical law embedded in the data, i.e. the steady state equations. Instead the inconsistency indicates that neither of the identified results contains a full set of relevant operators.

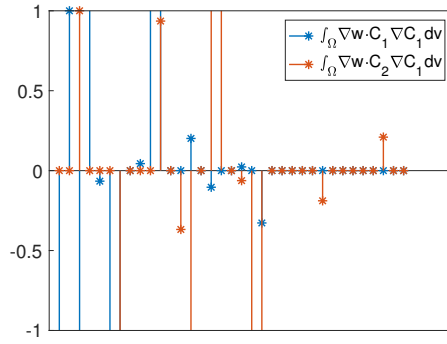


Figure 19: One example of inconsistently inferred operators with different target vectors using data at steady state. As shown in the figure, choosing $\int_{\Omega} \nabla w \cdot C_1 \nabla C_1 dv$ as target vector, $\int_{\Omega} \nabla w \cdot C_2 \nabla C_1 dv$ is turned on, but not vice versa.

On the other hand, choosing the relevant operators as the target vector will yield consistent results. The left plot in Figure 20 shows that the identified results are consistent up to a scaling factor, with 4 different operators as target vector. In fact the identified equation is the steady state equation of C_1 (i.e. the Equation (70)). Note that the operator $\int_{\Omega} w dv$ and $\int_{\Omega} w C_1 C_2^2 dv$ are two common operators in both equations (70) and (71). But choosing them as target vector only yields consistent operators in one equation with more operators. By eliminating the identified relevant operators $\int_{\Omega} \nabla w \cdot \nabla C_1 dv$ and $\int_{\Omega} w C_1 dv$ from the full candidate operator set, we are able to find the another set of consistent inferred operators, shown in left plot of Figure 20. This is also the steady state equation for C_2 .

In the following we choose the two diffusion operators, $\nabla^2 C_1$ and $\nabla^2 C_2$, as the target vectors

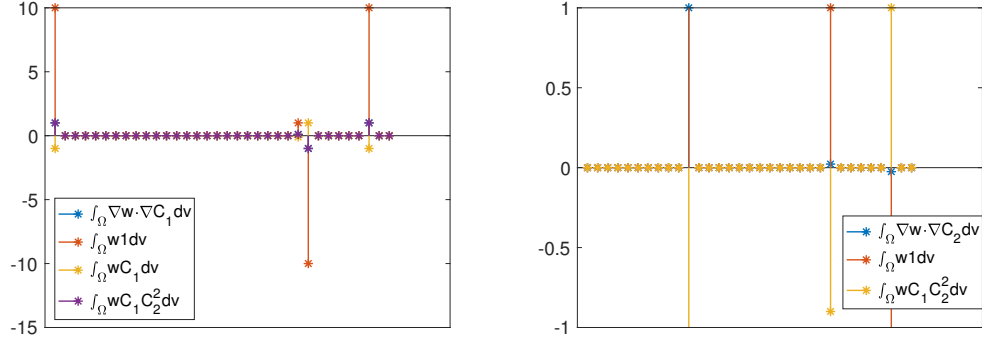


Figure 20: Two sets of consistent inferred operators with different target vectors using data generated from Model 1 at steady state. They are consistent up to a scaling factor. Note that the second set of consistent inferred operators is obtained on a reduced candidate operators library without $\int_{\Omega} \nabla w \cdot \nabla C_1 dv$ and $\int_{\Omega} w C_1 dv$, the two operators in the first set of consistent inferred operators. The two sets are the steady state equations for C_1 and C_2 in Equations (70) and (71), respectively.

and infer the remaining operators, $\tilde{\chi}$

$$\nabla^2 C_1 = \frac{1}{\omega_{D_1}} \tilde{\chi} \cdot \tilde{\omega} \quad (72)$$

$$\nabla^2 C_2 = \frac{1}{\omega_{D_2}} \tilde{\chi} \cdot \tilde{\omega} \quad (73)$$

Without noise, the high spatial resolution data yields very accurate results as shown in Figure (21) and (22) even with small snapshots. Then the scaling factors, ω_{D_1} and ω_{D_2} in Equations (72) and (73), i.e. the diffusion coefficients, are all correctly identified as shown in Table 3. The diffusion coefficients are not identifiable only using early time data collected from small snapshots as discussed before (See Figure 13).

| snapshot size | 400×400 | 300×300 | 200×200 | 100×100 | 50×50 |
|----------------|------------------|------------------|------------------|------------------|----------------|
| ω_{D_1} | 0.9998 | 0.9998 | 1.001 | 0.995 | 0.994 |
| ω_{D_2} | 39.95 | 40.01 | 40.02 | 39.72 | 39.23 |

Table 3: The identified scaling factor for governing equation of C_1 and C_2 using data generated from Model 1 with different size of snapshots.

Unlike diffusion-reaction equations that the formed pattern will become stable at steady state, Cahn-Hilliard equations behave differently. After the initial fast spinodal decomposition, the larger regions of cell clusters grow slowly at the expense of smaller ones. In fact after the initial spinodal decomposition, the evolution of concentrations is extremely slow (See Figure 23) , and thus the

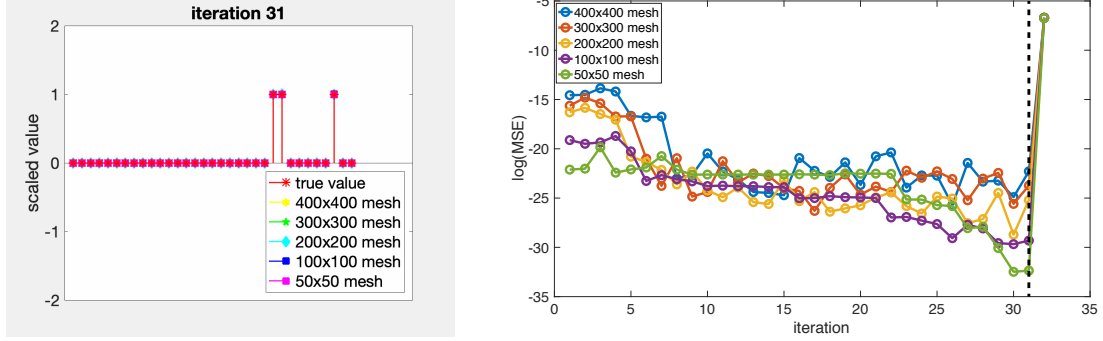


Figure 21: Inferred operators for C_1 (left panel) using data generated from Model 1 at steady state, and the loss (right panel) at each iteration. The identified coefficients of relevant terms are scaled by their true values. The algorithm converged at iteration 31 as the loss increases dramatically if any more operators are eliminated.

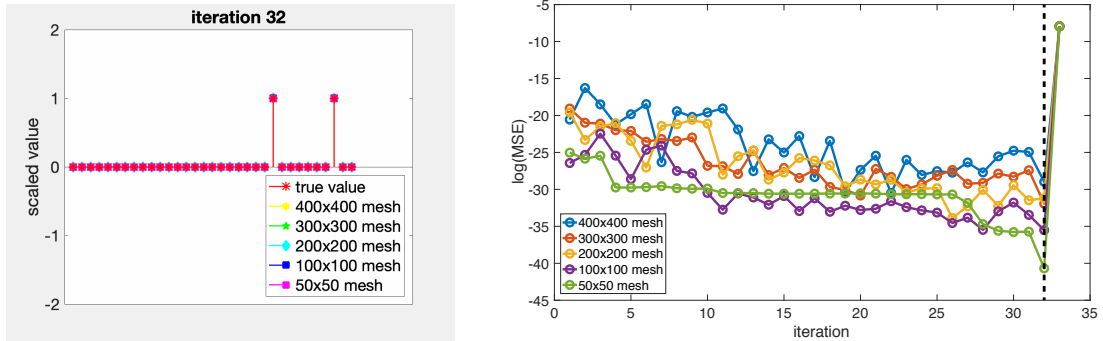


Figure 22: Inferred operators for C_2 (left panel) using data generated from Model 1 at steady state, and the loss (right panel) at each iteration. The identified coefficients of relevant terms are scaled by their true values. The algorithm converged at iteration 32 as the loss increases dramatically if any more operators are eliminated.

system is close to steady state:

$$\nabla \cdot (M_1 \nabla \mu_1) \approx 0 \quad (74)$$

$$\nabla \cdot (M_2 \nabla \mu_2) \approx 0 \quad (75)$$

We again find the sets of consistent inferred operators by examining the results of having all can-

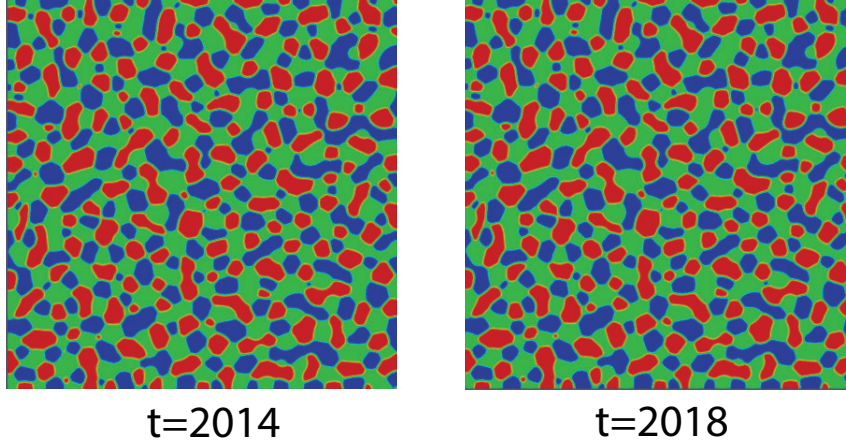


Figure 23: C_1 concentrations at two different times of Model 2. The Cahn-Hilliard equations evolves extremely slow after the initial spinodal decomposition. The system is close to steady state around $t=2018$.

didate operators to be target vector. Figure 24 shows the two sets of consistent inferred operators are found. Unlike the results of identifying the steady state equations for diffusion-reaction equations, choosing the common relevant operators would not favor to find one set of equations. This is because, we suspected, the two equations in Model 2 have same amount of operators and almost all of them are same. Besides due to the symmetry of free energy function (Equation (65)), the prefactors of these operators also show some "symmetry" in both equations (See Equation (68) and (69)). Again choosing two irrelevant operators to be target vector yields inconsistent inferred operators as shown in Figure 25.

In the following we choose the two biharmonic operators, $\nabla^4 C_1$ and $\nabla^4 C_2$, as the target vectors and infer the remaining operators, $\tilde{\chi}$

$$\nabla^4 C_1 = \frac{1}{\omega_{k_1}} \tilde{\chi} \cdot \tilde{\omega} \quad (76)$$

$$\nabla^4 C_2 = \frac{1}{\omega_{k_2}} \tilde{\chi} \cdot \tilde{\omega} \quad (77)$$

Without noise, the high spatial resolution data yields very accurate results as shown in Figure (26)

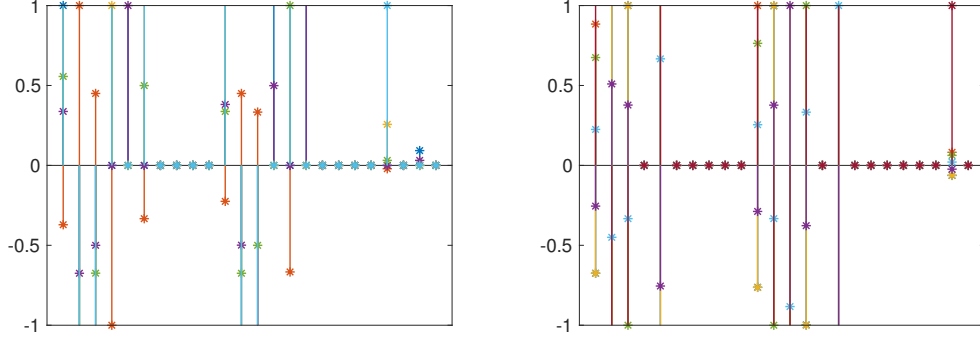


Figure 24: Two sets of consistent inferred operators with different target vectors using data generated from Model 2 at steady state. They are consistent up to a scaling factor. The target vectors in left panel are $\int_{\Omega} \nabla w \cdot \nabla C_1 dv$, $\int_{\Omega} \nabla w \cdot C_1 \nabla C_1 dv$, $\int_{\Omega} \nabla w \cdot C_1^2 \nabla C_1 dv$, $\int_{\Omega} \nabla w \cdot C_2^2 \nabla C_1 dv$, $\int_{\Omega} \nabla w \cdot C_1 C_2 \nabla C_2 dv$ and $\int_{\Omega} \nabla^2 w \nabla^2 C_1 dv$, and the target vectors in right panel are $\int_{\Omega} \nabla w \cdot C_2 \nabla C_1 dv$, $\int_{\Omega} \nabla w \cdot \nabla C_2 dv$, $\int_{\Omega} \nabla w \cdot C_1 \nabla C_2 dv$, $\int_{\Omega} \nabla w \cdot C_2 \nabla C_2 dv$, $\int_{\Omega} \nabla w \cdot C_1^2 \nabla C_2 dv$, $\int_{\Omega} \nabla w \cdot C_2^2 \nabla C_2 dv$ and $\int_{\Omega} \nabla^2 w \nabla^2 C_2 dv$.

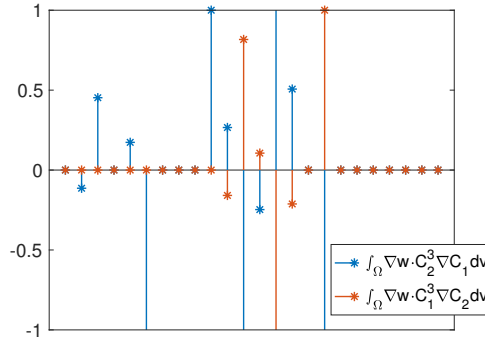


Figure 25: One example of inconsistently inferred operators with different target vectors using data generated from Model 2 at steady state. As shown in the figure, choosing $\int_{\Omega} \nabla w \cdot C_1^3 \nabla C_1 dv$ as target vector, $\int_{\Omega} \nabla w \cdot C_2 \nabla C_1 dv$ is turned on, but not vice versa.

and (27) even with small snapshots. Then the scaling factors, ω_{k_1} and ω_{k_2} in Equations (76) and (77), i.e. the coefficients for biharmonic operators, are all correctly identified as shown in Table 4.

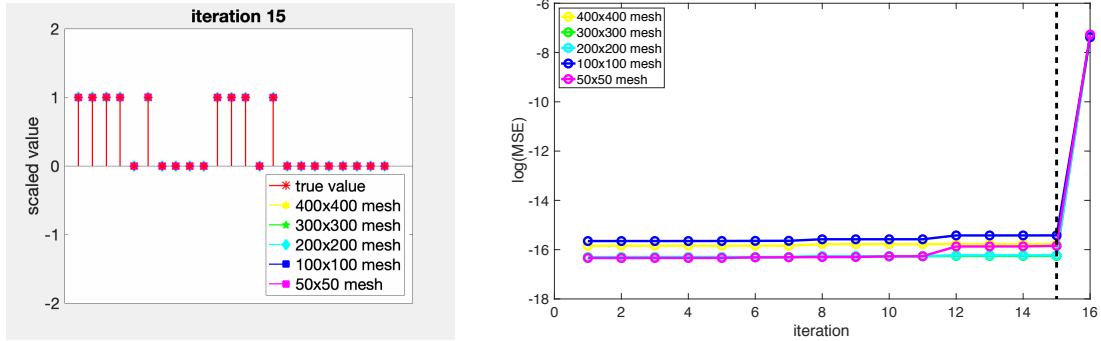


Figure 26: Inferred operators for C_1 (left panel) using data generated from Model 2 at steady state, and the loss (right panel) at each iteration. The identified coefficients of relevant terms are scaled by their true values. The algorithm converged at iteration 15 as the loss increases dramatically if any more operators are eliminated.

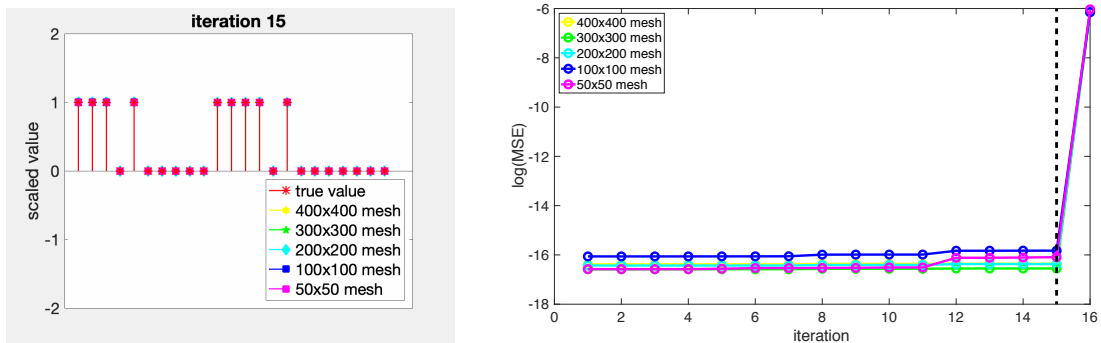


Figure 27: Inferred operators for C_2 (left panel) using data generated from Model 2 at steady state, and the loss (right panel) at each iteration. The identified coefficients of relevant terms are scaled by their true values. The algorithm converged at iteration 15 as the loss increases dramatically if any more operators are eliminated.

The noise in data would sabotage the results of Variational System Identification method. We didn't bother to study the noise effects here, as it has been illustrated thoroughly in our previous work[26].

| snapshot size | 400×400 | 300×300 | 200×200 | 100×100 | 50×50 |
|----------------|------------------|------------------|------------------|------------------|----------------|
| ω_{k_1} | 0.978 | 0.898 | 0.922 | 0.86 | 0.846 |
| ω_{k_2} | 0.994 | 0.91 | 0.91 | 1.08 | 1.27 |

Table 4: The identified scaling factor for governing equation of C_1 and C_2 using data generated from Model 2 with different size of snapshots. The true value is 1 for both factors.

4 Discussion and conclusions

The development of patterns in a many physical phenomena are governed by a range of spatio-temporal PDEs. It is compelling to attempt to discover the analytic forms of these PDEs from data, because doing so immediately provides insight to the governing physics. System identification has been explored using the strong form [25, 27, 28, 33, 34] and the weak form [26] of the PDEs as discussed in the Introduction. These techniques, however all need data that are spatially overlapping at multiple times in order to construct the time derivative operator. However, in materials physics in particular, the combination of heat treatment, processing and microscopy techniques results in datasets that are discordant with the PDE description of temporal evolution at fixed spatial locations. Microscopy data, therefore are only measured over subsets of the full domains, and the measured data at multiple times may come from different experiments/samples. The data hinders the use of system identification methods including SINDys and Variational System Identification. While other methods also discussed in the Introduction, are more flexible in their handling of data, they require many forward solutions of the PDEs. The computational expense makes it challenging to determine operators in PDEs from a comprehensive library of candidates.

For development of patterns in material physics, dynamic information can be measured from data collected from different samples and at different times. This is because of the statistical similarity of the patterns globally (See Figure 1, 4). Thus many statistical measurements, e.g. the moments of concentrations, can be well approximated using sample data. This justifies the use of the method of moments to extend Variational System Identification to incorporate spatially non-overlapping and sparse information. Data available from larger subsets of the full domain yield better approximations of the global quantities (See Figure 8 and 9). The poor approximations using small snapshots sabotage system identification, resulting in irrelevant operators being identified (See Figure 13). In practice, however, we may have much higher resolution of data in experiments than assumed here (smallest snapshots of 50×50) thus boosting the success of our methods.

We note that given few temporal snapshots, but high spatial resolution data, Variational System Identification can also pinpoint the complete governing equations of the dynamic system [26]. In fact, steady state data already provide most of the information about the system, up to only a scaling factor corresponding to kinetic coefficients such as diffusivities. In Section 3.5, we demonstrated that using data at steady state, we could identify all the operators in the PDEs up to a

constant scaling factor. Without prior knowledge it is challenging to choose relevant operators to be the target vector in our methods at steady state. However, by examining the consistency of the inferred operators using different candidates as the target vector, we were able to identify all the governing equations at steady state. Then identifying the single unknown in the original dynamic equations is reduced to a straightforward exercise with the method of moments. Thus, in cases wherein steady state (or near-steady state) data are available, they could be used as a “zeroth” step, followed by the additional two steps of the method of moments. However, if the dynamics remain far from steady state, the two-step method of moments is still applicable, given snapshots at sufficiently many time instants.

We note that Variational System Identification using the method of moments encompasses methods based on the principle of virtual work for the elasticity equations. The use of the Variational System Identification approach to discover strain energy functions from mechanical deformation data will appear in future communications.

Acknowledgements

We acknowledge the support of Toyota Research Institute, Award #849910, “Computational framework for data-driven, predictive, multi-scale and multi-physics modeling of battery materials” (ZW and KG). Additional support: This material is based upon work supported by the Defense Advanced Research Projects Agency (DARPA) under Agreement No. HR0011199002, “Artificial Intelligence guided multi-scale multi-physics framework for discovering complex emergent materials phenomena” (ZW, XH and KG).

References

1. T. Jiang, S. Rudraraju, A. Roy, A. Van der Ven, K. Garikipati, and M. L. Falk. Multi-physics simulations of lithiation-induced stress in litio electrode particles. *J. Phys. Chem. C*, 120, 2016.
2. S. Rudraraju, A. Van der Ven, and K. Garikipati. Mechano-chemical spinodal decomposition: A phenomenological theory of phase transformations in multi-component crystalline solids. *Nature Computational Materials*, 2, 2016.
3. G.H. Teichert, S. Rudraraju, and K. Garikipati. A variational treatment of material configurations with application to interface motion and microstructural evolution. *Journal of the Mechanics and Physics of Solids*, 99, 2017.
4. A. M. Turing. The chemical basis of morphogenesis. *Phil. Trans. Roy. Soc. Lond. Ser. B.*, 237, 1952.
5. A. Gierer and H. Meinhardt. A theory of biological pattern formation. *Kybernetik*, 12, 1972.

6. J. D. Murray. On pattern formation mechanisms for lepidopteran wing patterns and mammalian coat markings. *Phil. Trans. Roy. Soc. Lond. Ser. B*, 295, 1981.
7. R. Dillon, P. K. Maini, and H. G. Othmer. Pattern formation in generalized turing systems i: Steady-state patterns in systems with mixed boundary conditions. *J. Math. Biol.*, 32, 1994.
8. R. A. Barrio, C. Varea, and J. L. Aragon. A two-dimensional numerical study of spatial pattern formation in interacting turing systems. *Bull. Math. Biol.*, 61, 1999.
9. R. A. Barrio, R. E. Baker, B. Vaughan, K. Tribuzy, M. R. de Carvalho, Rodney Bassanezi, and P. K. Maini. Modeling the skin pattern of fishes. *Phys. Rev. E*, 79, 2009.
10. Philip K. Maini, Thomas E. Woolley, Ruth E. Baker, Eamonn A. Gaffney, and S. Seirin Lee. Turing’s model for biological pattern formation and the robustness problem. *Interface Focus*, 2(4):487–496, 2012. doi: 10.1098/rsfs.2011.0113.
11. F. Spill, P. Guerrero, T. Alarcon, P. K. Maini, and H. Byrne. Hybrid approaches for multiple-species stochastic reaction-diffusion models. *J. Comput. Phys.*, 299, 2015.
12. K. Korvasová, E. A. Gaffney, P. K. Maini, M. A. Ferreira, and V. Klika. Investigating the turing conditions for diffusion-driven instability in the presence of a binding immobile substrate. *J. Theor. Biol.*, 367, 2015.
13. K. Garikipati. Perspectives on the mathematics of biological patterning and morphogenesis. *J. Mech. Phys. Solids.*, 99, 2017.
14. J. W. Cahn and J. E. Hilliard. Free energy of a nonuniform system. i interfacial energy. *J. Chem. Phys.*, 28, 1958.
15. S. M. Wise, J. S. Lowengrub, H. B. Frieboes, and V. Cristini. Three-dimensional multispecies nonlinear tumor growth–model and numerical method. *J. Theor. Biol.*, 253, 2008.
16. V. Cristini, X. Li, J. S. Lowengrub, and S. M. Wise. Nonlinear simulations of solid tumor growth using a mixture model: invasion and branching. *J. Math. Biol.*, 58, 2009.
17. J. S. Lowengrub, H. B. Frieboes, F. Jin, Y-L. Chuang, X. Li, Macklin, S. M. Wise, and V. Cristini. Nonlinear modelling of cancer: bridging the gap between cells and tumours. *Nonlinearity*, 23, 2010.
18. J. S. Lowengrub, A. Rätz, and A. Voigt. Phase-field modeling of the dynamics of multicomponent vesicles: Spinodal decomposition, coarsening, budding, and fission. *Phys. Rev. E*, 79, 2009.

19. G. Vilanova, I. Colominas, and H. Gomez. Capillary networks in tumor angiogenesis: From discrete endothelial cells to phase-field averaged descriptions via isogeometric analysis. *Num. Meth. Biomed. Eng.*, 29, 2013.
20. G. Vilanova, I. Colominas, and H. Gomez. Coupling of discrete random walks and continuous modeling for three-dimensional tumor-induced angiogenesis. *Comput. Mech.*, 53, 2014.
21. J. T. Oden, A. Hawkins, and S. Prudhomme. General diffuse-interface theories and an approach to predictive tumor growth modeling. *Math. Mod. Meth. App. Sci.*, 20, 2010.
22. J. Xu, G. Vilanova, and H. Gomez. A mathematical model coupling tumor growth and angiogenesis. *PLoS ONE*, 11, 2016.
23. R. HilleRisLambers, M. Rietkerk, F. van den Bosch, H.H.T. Prins, and H. de Kroon. Vegetation pattern formation in semi-arid grazing systems. *Ecol.*, 82:50–61, 2001.
24. M. Rietkerk and J. van de Koppel. Regular pattern formation in real ecosystems. *Trends Ecol. Evol.*, 23:169–175, 2008.
25. S. L. Brunton, J. L. Proctor, and J. N. Kutz. Discovering governing equations from data by sparse identification of nonlinear dynamical systems. *Proc. Natl. Acad. Sci.*, 113, 2016.
26. Z. Wang, X. Huan, and K. Garikipati. Variational system identification of the partial differential equations governing the physics of pattern-formation: Inference under varying fidelity and noise. *Computer Methods in Applied Mechanics and Engineering*, 356:44 – 74, 2019. ISSN 0045-7825. doi: <https://doi.org/10.1016/j.cma.2019.07.007>.
27. N. M. Mangan, S. L. Brunton, J. L. Proctor, and J. N. Kutz. Inferring biological networks by sparse identification of nonlinear dynamics. *IEEE Trans. Mol. Biol. Multi-Scale Commun.*, 2, 2016.
28. S. H. Rudy, S. L. Brunton, J. L. Proctor, and J. N. Kutz. Data-driven discovery of partial differential equations. *Sci. Adv.*, 3, 2017.
29. M. Raissi, P. Perdikaris, and G.E. Karniadakis. Physics-informed neural networks: A deep learning framework for solving forward and inverse problems involving nonlinear partial differential equations. *J. Comput. Phys.*, 378, 2019.
30. J. Cottrell, T. Hughes, and Y. Bazilevs. Isogeometric analysis: Toward integration of cad and fea. *Wiley, Chichester*, 2009.
31. G. James, D. Witten, T. Hastie, and R. Tibshirani. An introduction to statistical learning. *Springer New York, Inc., New York, NY, USA.*, 2013.

32. J. Schnakenberg. Network theory of microscopic and macroscopic behavior of master equation systems. *Rev. Mod. Phys.*, 48, 1976.
33. M. Schmidt and H. Lipson. Distilling free-form natural laws from experimental data. *Science*, 03, 2009.
34. M. D Schmidt, R. R Vallabhajosyula, J. W Jenkins, J. E Hood, A. S Soni, J P Wikswo, and H. Lipson. Automated refinement and inference of analytical models for metabolic networks. *Phys. Biol.*, 8, 2011.